3.3 A new method using repeated OPTV records to reconstruct "in-situ" submergence velocities and vertical strain rates of firn and ice at Derwael ice rise and related applications

3.3.1 High-resolution vertical velocity and strain rates reconstructed from optical televiewer-based layer differencing: Derwael ice rise, East Antarctica

Paper submitted to Geophysical Research Letters, 2017

Title: High-resolution vertical velocity and strain reconstructed from optical televiewer-based layer differencing: Derwael ice rise, East Antarctica

Authors: Morgane Philippe[1], Bryn Hubbard[2], Frank Pattyn[1], Reinhard Drews[3], Karen Fjøsne[1], Carine Bruyninx[4], Nicolas Bergeot[4], Jean-Louis Tison[1]

[1] Laboratoire de Glaciologie, Département des Géosciences, Environnement et Société, Université libre de Bruxelles, 1050 Brussels, Belgium
[2] Centre for Glaciology, Department of Geography and Earth Sciences, Aberystwyth University SY23 3DB, UK
[3] Department of Geosciences, University of Tübingen, Wilhelmsstraße 56, 72074 Tübingen, Germany
[4] Koninklijke Sterrenwacht van België/Observatoire Royal de Belgique, Ringlaan 3, 1180 Brussels, Belgium
Corresponding author: Morgane Philippe (mophilip@ulb.ac.be)

Key Points:

- Repeat optical televiewer-based layer differencing records mm-scale vertical velocity in firn and ice.
- Deriving vertical velocity at Derwael Ice Rise yields discretized vertical strain over the uppermost ~100 m.
- Capturing vertical variability in strain rates will improve age-depth and annual layer thickness reconstructions

Abstract

Direct measurements of vertical strain within ice masses are scientifically valuable but challenging to acquire. Here we derive relative vertical velocities of 60 markers imaged by optical televiewer (OPTV) in 2012 and repeated in 2014 at millimetric resolution along a borehole drilled into the dome of Derwael Ice Rise, East Antarctica. An absolute vertical velocity profile is compiled using local submergence velocity measured by GNSS at the ice surface. Vertical strain rates are calculated between successive markers as the derivative of the vertical velocity with depth. Following regularization of the derivative to reduce error-related variability, the resulting 100 m-long strain rate profile decays as inverse of depth, consistent with values from three adjacent coffee-can experiments and generally matching that predicted by an ice-flow model. Slight model under-prediction of strain rates is interpreted in terms of the model's assumption of constant surface accumulation, which is known in reality to have increased through the 20th century in particular.

3.3.1.1 Introduction

3.3.1.1.1 Background

Evaluating the contribution of ice masses to sea-level rise requires knowledge of surface mass balance (SMB). Although SMB can be measured directly by site-based methods such as snow pit stratigraphy, snow/firn core stratigraphy, sonic depth data, and ablation stake data, such measurements are logistically demanding and constrained by often-poor accessibility. In contrast, studies assessing the overall ice sheet mass change, often rely on more widespread satellite-based measurements of surface elevation change (Davis et al., 2005). However, this method depends on the accurate constraint of other contributing processes such as firn densification, lateral ice deformation, and isostatic rebound (e.g., Spikes et al., 2003). The first two of these reduce to vertical strain within the snow, firn and ice column. Such measurements can also be used to improve model-based ice core chronologies, to reconstruct age-depth relationships in the absence of clear annual layering (e.g., Hawley et al., 2002), and to guide depth-density functions (e.g., Kingslake et al., 2016). Horizontal gradients in vertical strain rate are also responsible for the development of isochrone arches in the stratigraphy of ice rises (Raymond, 1983; Matsuoka et al., 2015). Despite this value, however, vertical strain rate profiles are difficult to measure directly and such measurements are correspondingly scarce. Thus, the overwhelming majority of SMB reconstructions from measurements of annual layer thicknesses have, to date, included model-based approximations of vertical strain (e.g., Thomas et al., 2008), assumed to be either constant (Nye, 1963) or constant near the surface and decreasing at depth (Dansgaard and Johnsen, 1969), when they are not guided by a full-Stokes model taking into account the Raymond effect (e.g. Drews et al., 2015, used in Philippe et al., 2016). Thus, the non-linearity of vertical strain, particularly near ice divides, is not fully captured by current ice-flow models (Kingslake et al., 2014).

The 'coffee-can' method (CCM) was developed by Hamilton et al. (1998) to measure vertical strain directly within ice masses. Here, a marker is fixed at depth in the firn column and its vertical displacement recorded over time relative to a reference point located at or near the surface. Although originally based on fixed poles, the technique now normally involves measuring the length of pre-tensioned cable retrieved over a wheel mounted on a surface reference datum such as a glacio-pole, although fibre-optic cable stretch has also been recorded for this purpose (e.g., Zumberge et al., 2002). Cable retrieval is measured either during repeated site visits or automatically at higher temporal resolution by a depth encoder attached to the surface spool (e.g., Arthern et al., 2010). Although valuable and easy to implement, the technique is prone to error from factors such as pole bend or tilt, mechanical friction, influence of wind on the cable, lateral strain within the installation borehole, and anchor slippage. All such 'surface-to-marker' measurements also provide only a mean strain rate over the full length separating the surface reference from the marker.

There is therefore a need for precise measurements of spatially-distributed strain between closely-spaced markers covering the full depth range of interest. While distributed fibre-optic analysis has been used to measure discretized strain along terrestrial surfaces (e.g., Moore et al., 2010), and has great potential, the ability of the technique to record distributed vertical strain in ice boreholes has not yet been demonstrated. At least three other techniques have gone some way to this end. First, phase-sensitive radio echo sounding (pRES) has recently been developed with the capacity to record the depth of radar layers at high spatial resolution (e.g., Gillet-Chaulet et al., 2011; Kingslake et al., 2014; Martin et al., 2015). Repeating pRES surveys at a given location can therefore be used to difference the thicknesses of individual layers to produce vertical profiles of spatially-discrete vertical strain and velocity across the full depth of radar wave penetration. For example, Kingslake et al. (2014) measured englacial vertical velocities within ice divides up to 900 m thick, and studied spatial variations in vertical strain rates along transects of a few kilometers across Berkner Island, Roosevelt Island, Fletcher Promontory and Adelaide Island. This technique has many advantages specific to radar in general: logistical ease, large spatial coverage, etc. However, the precision of pRES is still restricted by several factors, especially below ~50m, including (i) temporal changes in material properties that influence radar wave velocity and thus inferred depth; (ii) limits to radar wave penetration, and (iii) slight variations in ray-path alignment between surveys. Second, Raymond et al. (1974) installed 14 metal collars at depths of up to 226 m in a borehole drilled into the Dyer Plateau, Antarctica, and measured their depths separated by a period of 2 years. While differencing these depths did yield vertical strain data, the technique was found to be logistically demanding and subject to errors associated with collar emplacement and slippage. The technique also provides a limited number of observations, and cannot be used in irregularly-walled boreholes such as those drilled by hot water. Third, Hawley and Waddington (2011) measured vertical strain from repeated measurement of natural layers recorded in optical logs of a borehole drilled to a depth of ~30 m at Summit, Greenland. These authors reported firn compaction using a downward-looking borehole camera on the basis of three, annually-repeated logs. The resulting vertical velocity profile matched closely that predicted by a compaction model based on measured densities and an assumption of steady surface accumulation over the ~70-year time period concerned. Although representing a notable advance, the use of a downward-looking camera that was not always centered in the borehole resulted in feature blurring. Stratigraphic logs were therefore low-pass filtered, with a threshold of 0.075 m, and their luminosity traces differenced by a cross correlation function applied separately to several 0.5 m-long reference sub-sections. Although somewhat limited by the camera technology available at the time, the repeat logging approach of Hawley and Waddington (2011) has the capacity to yield high resolution firn compaction data. Importantly, borehole optical televiewing (OPTV) overcomes these key technological limitations and forms the basis of the research presented here.

We apply repeat OPTV logging to a ~120 m-deep borehole located on the dome of Derwael Ice Rise (DIR), East Antarctica. The relative movement of individual identifiable markers is recorded over two years and combined with GNSS-based measurements of vertical velocity at the surface to produce the DIR's vertical velocity profile. These data are compared with coffee can measurements recorded over three depth ranges. Vertical strain rates are calculated between successive markers as the derivative of the vertical velocity with depth. We use the total-variation regularization method (Chartrand, 2011) to reduce error-related variability in these spatially-distributed strain rates. The same method is applied to ice equivalent vertical velocity to assess the ability of an ice flow model to predict the vertical strain rate profile.

3.3.1.2 Field site and methods

3.3.1.2.1 Field site, ice coring and surface positioning

The study site is located at the dome of ~550 m-thick Derwael Ice Rise (DIR) (Drews et al., 2015) in coastal Dronning Maud land, East Antarctica (Figure 3.3.1.1). A ~120 m-long ice core ('IC12') was recovered from the site by Eclipse electro-mechanical corer in late 2012. Annual layer counting based on $\delta^{18}O$ and δD, major ion concentration and electrical conductivity, was used to date the core, the base of which was 1759 A.D. (Philippe et al., 2016). These authors also measured ice-core density gravimetrically (i.e. measured directly from the mass of core samples of known volume), supplemented by OPTV-based estimates following Hubbard et al. (2013). Combining the density and annual layer data allowed the DIR's long-term accumulation record to be reconstructed, reported by Philippe et al. (2016) as 0.52 ± 0.01 m ice equivalent a^{-1} over the full time period concerned. This record also showed an increasing trend, particularly since the mid-20th century, such that mean accumulation at DIR for the period 1992-2011 had increased to 0.70 ± 0.01 m ice equivalent a^{-1}.

A GNSS station ('ROB1') was installed within a few 10s of meters of IC12 to measure daily surface position from late 2012 to early 2016. The antenna position, initially anchored at a depth of 1.85 m, was determined using Bernese 5.2 software (Dach et al., 2015). Processing was based on GNSS position referenced, via long-term and overlapping GPS and GLONASS data (Dow et al., 2009), to the global ITRF2014 (International Reference Frame 2014, Altamimi et al, 2016). Vertical velocity was calculated by stacking the daily solutions using CATREF (Combination and Analysis of Terrestrial Reference Frames Software, Altamimi et al., 2007) and modeling the annual signal, yielding a mean submergence velocity through 2013 and 2014 of -1.380 ± 0.009 m a^{-1}.

A hexagonal strain network was established using eight markers located along a circle of 2 km radius around the dome. These markers were positioned using differential GNSS in 2012 and 2013. Lateral divergence is calculated from orthogonal horizontal strain rates ($\dot{\varepsilon}_{xx}$ and $\dot{\varepsilon}_{yy}$) between two pairs of markers, located on perpendicular axes crossing at the dome. Based on the principle of mass conservation ($-\dot{\varepsilon}_{zz} = \dot{\varepsilon}_{xx} + \dot{\varepsilon}_{yy}$), the measured vertical strain rate at the surface is -2.2 ± 0.2 10^{-3} a^{-1}.

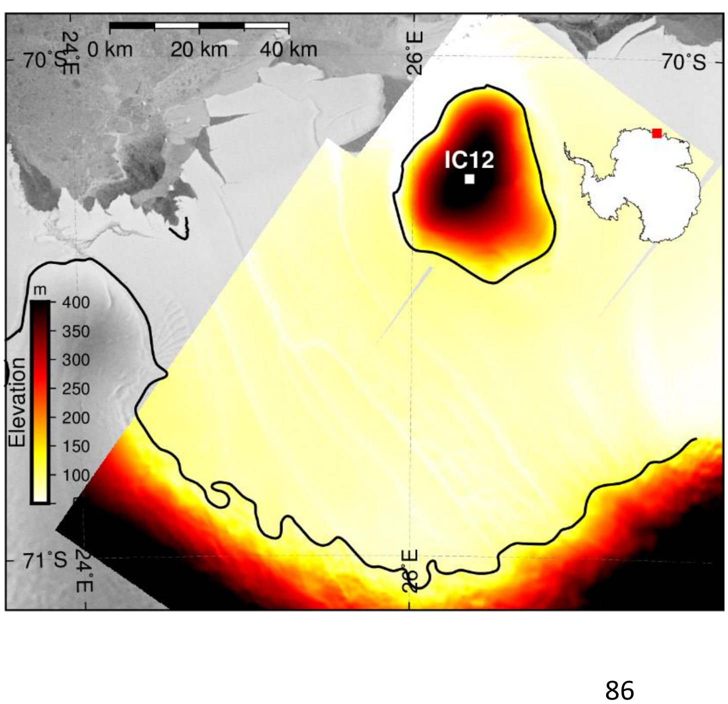

Figure 3.3.1.1. Study site location. Background is from Radarsat (Jezek and RAMP-Product-Team, 2002). Elevation is from TanDEM-X (Lenaerts et al., 2017). Grounding lines are combined from Depoorter et al. (2013), the Antarctic Digital Database and Berger et al. (2016).

3.3.1.2.2 Borehole optical televiewing and layer thickness change

OPTV records a geometrically-accurate colour image of the complete wall of any logged borehole. The OPTV sonde used for this study illuminates the borehole wall with an outward-facing circular array of 72 white LEDs, the luminosity of which can be controlled by the operator. The image is recorded by a CCD (charge-coupled device) camera that records the lateral 360° pixel row of the adjacent borehole wall (Hubbard et al., 2008; 2012). Pixel rows are recorded at tightly-controlled depth steps as the sonde is lowered or raised along the borehole. The resulting OPTV logs, recorded for this study initially in December 2012 and again in December 2014, have a lateral resolution of ~1.5 mm and a vertical resolution of 1 mm in 2012 and 2 mm in 2014, the former of which was sub-sampled to 2 mm for consistency. The OPTV logs used herein include the uppermost 99.86 m of IC12 because the ~20 m-long section below this was scored by cutters during drilling in 2012, artificially degrading the log's luminosity trace (as described by Hubbard et al., 2013). OPTV logs were analyzed using the Borehole and Ice Feature Annotation Tool (BIFAT) (Malone et al., 2012) and commercial WellCAD software. Once acquired, the 2014 log was shifted vertically to the common datum of the borehole top in 2012. We calculate OPTV luminosity as the mean brightness intensity recorded around each pixel row.

To facilitate the precise calculation of distributed strain rates and vertical velocities from which they are derived, we define 60 reference markers used as tie points for comparison between the two OPTV logs. These points were defined on the basis of being (i) clearly identified as sharp peaks or troughs in the luminosity trace of both logs, and (ii) separated by at least 1 m, optimizing the length over which vertical strain is measured. Including the surface, these markers separate 60 layers, with a mean thickness of 1.66 m. Relative vertical velocity was calculated from the depth differences of these 60 markers that occurred over two years (further detailed in Sect. 3.3.1.2.4).

Although the depth encoder linked to the OPTV's cable has a precision of ~0.04 mm, the system is also subject to operational error in recording exact feature depth. In order to evaluate this error, we logged IC12 two times on the same day (and in the same upward direction) and compared the apparent displacement of the study's 60 markers relative to a common datum. This comparison yields a depth-independent, normal distribution (p-value = 0.364) of residuals of standard deviation 3.78 mm (Figure S.3.3). The most likely causes of this mm-scale error are (i) variations in the centre-point depth of markers defined by more than 1 pixel (2 mm), (ii) OPTV probe wobble, and (iii) variability in cable tension and elastic response between the two logs. Hereafter, we take this (1 s.d.) length of 3.78 mm (which translates to a velocity error of 3.78 mm over the two-year time period) to represent the error associated with repeated OPTV-based measurements of feature depth.

3.3.1.2.3 Coffee can method

The coffee-can method (CCM) involves installing an anchor at a known depth within a borehole and recording its displacement through time relative to a fixed, near-surface datum (Section 3.3.1.1.1, above) (Hamilton and Whillans, 2000). As noted above, anchor slippage, identified as an unfeasibly large strain, is not uncommon in CCM experiments and two coffee cans were omitted from the current study for this reason. All anchors were installed in separate boreholes, each drilled within 50 m of the IC12 borehole. The three anchors that held firm were installed at depths of 12.00 m, 21.70 m and 42.35 m and their depths were recorded ~12 months apart in December 2012 and again in December 2013. The resulting data are expressed as vertical strain averaged over the distance separating successive anchors, although they are located in different boreholes, to enable comparison with the OPTV-derived strain rates. Considering two of our five CCM experiments experienced anchor slippage, we adopt a depth uncertainty for this study of 200 mm.

3.3.1.2.4 Submergence velocity and vertical strain rates

Relative vertical velocity is calculated as the depth difference of each marker between two measurements (2012 vs. 2014) divided by the time period separating those measurements, ~2 years (720 days) in this study. Since depth is measured relative to the 2012 surface, the absolute velocity of each marker is given by subtracting its (upward) velocity from the (downward) velocity measured at the surface (-1.38 m a^{-1}, Section 3.3.1.2.1 above).

The vertical strain rate $\dot{\varepsilon}_{zz}(z)$ is calculated as the derivative of the vertical velocity *w(z)* along the z axis, which is equivalent to the difference in layer thickness "l" (delimited by two successive markers) between the two observational years (t_1 and t_2) divided by the distance over which the strain rate is measured (initial layer thickness l_1 between two successive markers, i.e. *dz)* and the time separating the measurements (Eq. 3.3.1.1).

$$\dot{\varepsilon}_{zz}(z) = \frac{dw(z)}{dz} = \frac{(l_2 - l_1)}{l_1 * dt} = \frac{(l_2 - l_1)}{dz * dt} \qquad \text{Eq. 3.3.1.1}$$

OPTV-reconstructed vertical velocities have an estimated standard deviation of 0.008 m a^{-1}, which amplifies the noise in the corresponding strain rates when these are calculated with Eq. 3.3.1.1. We reduce this noise by applying total-variation regularization, which accounts for noisy data by using an inverse method for differentiation (Chartrand, 2011). We chose the regularization parameter (i.e. the smoothness of the vertical strain rate profile) such that the corresponding regularized velocity values are within one standard deviation of the measured data.

Ice-equivalent vertical strain rates are calculated for comparison with modelled strain rates (Section 3.3.1.2.5) and are derived from ice-equivalent velocities, using the depth-density profile of Hubbard et al. (2013) for IC12 (DIR) and assuming that this profile is in steady-state between 2012 and 2014. The 2012 surface was located at a depth of 2.82 m beneath the 2014 surface.

Since the vertical velocity profile reported here is relative to the 2012 surface, we consider a directional 5 cm error to account for additional compaction due to the weight of the wooden board covering the borehole of 2012. This error also affects the uppermost strain rate datum, as it is computed between the first marker and this (2012) surface. Below that first measurement, errors on strain rates are calculated using standard error propagation to account for the 3.78 mm error affecting both 2012 and 2014 marker depths. Uncertainties in the density profiles are not independent and are therefore not included in the error analysis for the 'ice equivalent' vertical strain rates. These are, however, affected by the different depth ranges over which density is calculated.

3.3.1.2.5 Ice-flow modelling

We compare our empirically-reconstructed strain rate and vertical velocity data (in ice equivalent), with simulated values for DIR based on a 'full Stokes' solution of Drews et al. (2015) taking into account ice anisotropy (n = 3) and a small amount of surface lowering (0.03 m a^{-1} over 3400 years). The modeled vertical velocity profile was scaled to match the vertical strain rate at the surface derived from the lateral divergence measured by the strain network (Section 3.3.1.2.1 above, Philippe et al., 2016).

3.3.1.3 Results

3.3.1.3.1 Strain rates determined by OPTV layer differencing

The 2012 and 2014 OPTV logs of IC12 are presented in Figure 3.3.1.2a and b. Both logs are remarkably similar overall, showing a general decrease in luminosity with depth and the presence of numerous horizontal layers. The former effect has been interpreted as reduced material reflectivity through snow metamorphism to ice (Hubbard et al., 2013) and the latter as annual layering (e.g., Hubbard et al., 2012; Hubbard and Malone, 2013). However, it is likely that the anomalously large excursions towards lower luminosity, e.g. at depths of 5, 17 and 35 m, correspond to infiltration ice layers resulting from substantial surface melt events. It is also apparent from inspection of the raw OPTV images shown in Figure 3.3.1.2 that these three infiltration ice layers become displaced vertically from each other during the 2-year period separating the logs, providing a visual illustration of firn column compression.

The infiltration ice layers noted above represent three of the 60 marker horizons used to calculate velocities and strain rates in the uppermost 100 m of IC12. We illustrate this analysis by focusing on a 6.6 m-long section of the OPTV logs, the luminosity profiles of which are presented in Figure 3.3.1.2c to e. In Figure 3.3.1.2c, the luminosity traces of both logs, aligned to the same (summer 2012) surface datum, are overlaid. While the magnitude of these profiles corresponds closely, individual roughness features, principally annual layers in this section, do not match. In Figure 3.3.1.2d, this 6.6. m section of the 2012 log has been raised to align it with one particular positive peak located near the top of the 2014 log at a depth of ~59.05 m. With this additional local alignment, the remarkable overall similarity of the two OPTV logs becomes apparent. Individual peaks and troughs match almost precisely at millimetric scale, illustrating the capability of the OPTV-based method for matching layers at very high spatial resolution. Further, even over this 6.6 m-long section, a progressive offset with depth is apparent as the 2014 luminosity trace compresses relative to the 2012 trace. This offset increases down-section, such that the initial offset of zero near its top increases to ~60 mm near its base, resulting in a local vertical strain rate of ~-0.005 a^{-1}. In Figure 3.3.1.2e, the local depth alignment is once again removed and the luminosity traces separated laterally (note the different x-axes) to allow illustration of the offset of the five (of 60 in total) markers used in our analysis that are located within this section, traced by dotted lines in Figure 3.3.1.2e. The total offset is ~1.5 m at this depth, resulting from the total strain between here and the surface over the two years separating the logs.

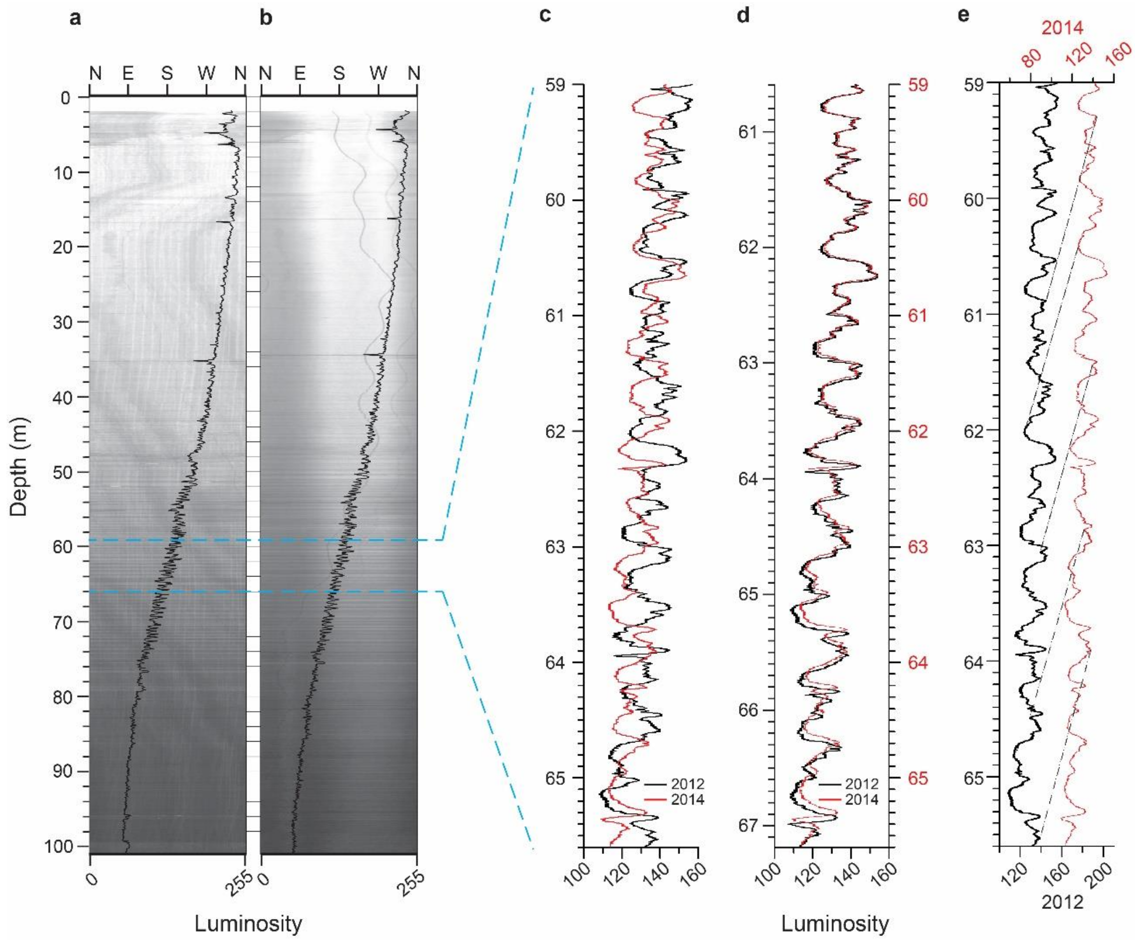

Figure 3.3.1.2. Raw OPTV logs with overlaid luminosity traces for (a) the DIR borehole in 2012 and (b) the DIR borehole in 2014 (not including new snow accumulation). Note that the quasi vertical streaks are caused by scoring of the borehole walls by corer and/or OPTV probe centralizers. (c) Expansion of OPTV luminosity logs between 59.0 and 65.6 m illustrating both logs (black line = 2012, red line = 2014) on the same depth scale measured from the borehole top in 2012; (d) Both logs as in (c) but with the 2012 log additionally raised to match the 2014 log at the top of the expansion. (e) Both logs as in (c) but separated laterally to illustrate five of the 60 markers used as tie points in the analysis. Note the offset between the two logs increases slightly down the expansion due to compressive strain between 2012 and 2014, particularly evident in panels (d) and (e).

Figure 3.3.1.3a shows vertical velocities of the 60 OPTV markers calculated as described in section 3.3.1.2.4. It shows a general logarithmic decrease with depth (which includes the effect of snow densification), of Eq. 3.3.1.2 (R^2=0.99), yielding a value of ~0.6 ± 0.1 m a^{-1} at the 100 m-deep base of OPTV logs (Figure 3.3.1.3a).

$$w = 0.21\ln(z) - 1.425 \qquad \text{Eq. 3.3.1.2}$$

where w is the vertical velocity (m a^{-1}) and z is the depth (m).

Strain rates, calculated here as the derivative of the velocity at each marker, are plotted against depth in Figure 3.3.1.3b. They show a steep decay near the ice-rise surface and substantial inter-layer variability along the full length of the borehole. We remove the error-related component of this variability by regularizing the strain-rate derivative (Section 3.3.1.2.4 above), resulting in a smoother strain-rate profile (green line in figure 3.3.1.3a) corresponding to a regularized velocity profile (green line in figure 3.3.1.3b) fitting within the error bars of the observed discrete velocity profile. Nonetheless, notable inter-layer variability in discretized strain rate remains.

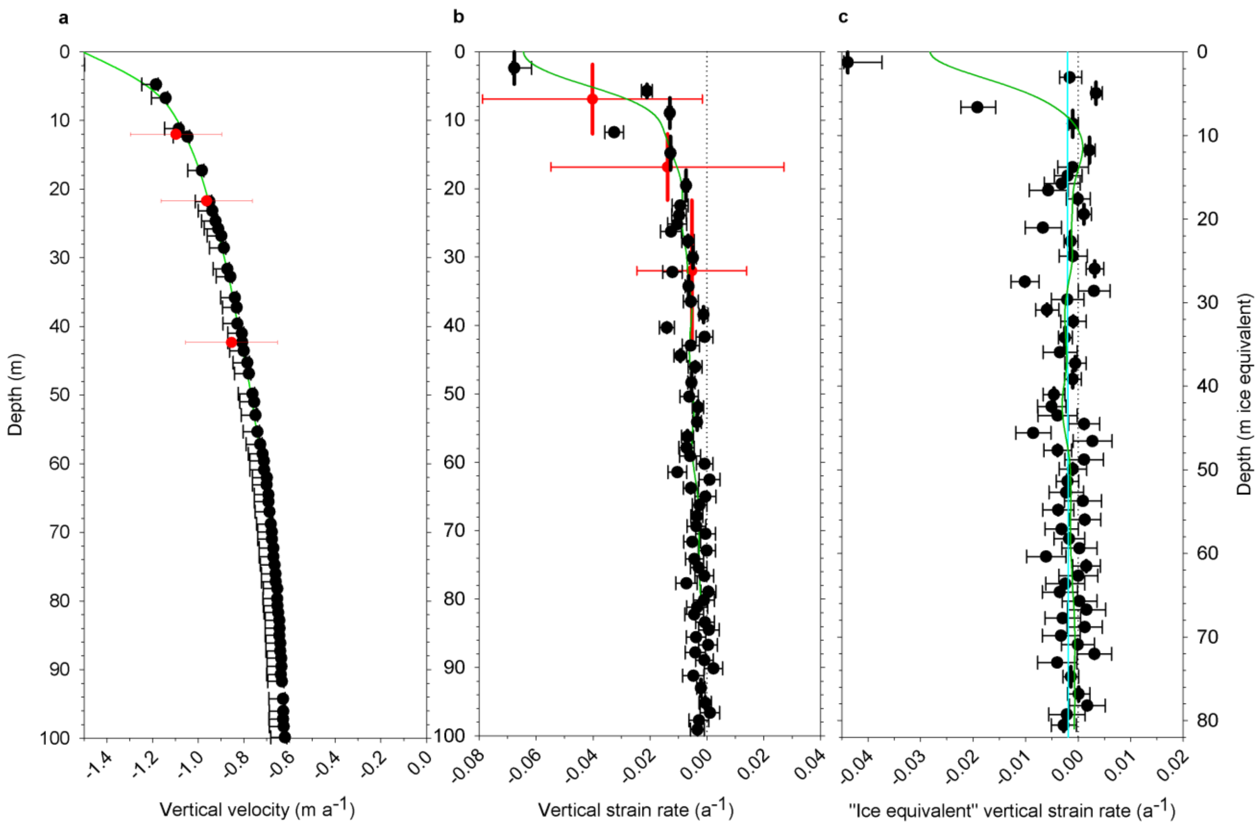

Figure 3.3.1.3. Measured and modelled vertical strain rates and vertical velocities beneath the crest of DIR. (a) Vertical velocities reconstructed from combining the layer thickness changes relative to the surface with the local surface submergence velocity measured by GNSS, with associated 5 cm directional error bars for OPTV-based layer differencing (black dots) and 20 cm error bars for the coffee-can method (red dots). (b) Vertical strain rates reconstructed from the derivatives of the vertical velocities presented in (a), with associated horizontal error bars (see text for details). Vertical bars reflect the depth over which the strain is calculated. The green line represents the data following regularization of the derivative to remove variability due to error. (c) Same as (b) but the vertical strain rates are derived from ice-equivalent vertical velocities for comparison with modelled strain rates. The blue line represents the values predicted by modelled ice flow.

3.3.1.3.2 Strain rates and vertical velocities determined by the coffee can method

The results of the three CCM experiments are superimposed on the OPTV-based data in Figure 3.3.1.3a and b. These data highlight the longer distances over which the CCM strain rates are measured, the scarcity of the measurements and the large error bars associated with this method. Nonetheless, the results yielded by both methods correspond closely.

3.3.1.3.3 Modelled vertical strain profile

The vertical strain rate profile predicted by the flow model of Drews et al. (2015) is broadly consistent with our OPTV-based spatially-distributed strain rates (Figure 3.3.1.3c). In particular, the mean strain rate derived from our OPTV-measured vertical velocities below the firn ice transition (0.0019 a^{-1} below ~65 m) is equal to the mean strain rate predicted by the model in the uppermost 100 m, lending general support to the model's structure and boundary conditions.

After taking densification into account, observed strain rates remain systematically larger than the modelled ones. The average observed strain rate is 0.0025 a^{-1}, while the averaged modelled strain rate is 0.0019 a^{-1}. Also, the model shows no variability in strain rate with depth, while a variability of 0.005 a^{-1} (1 standard deviation) remains in the regularized 'ice equivalent' strain rate profile.

3.3.1.4 Discussion and conclusions

Two OPTV-based luminosity profiles of the IC12 borehole, recovered initially in late 2012 and subsequently in late 2014, reveal remarkable millimetric-scale similarity in the detail of imaged markers. Differencing 60 distinctive layers between successive markers in both logs has allowed the reconstruction of a high-resolution, spatially-distributed vertical strain profile, indicating rates of up to 0.07 a^{-1} near the surface, decaying logarithmically to values of ~0.008 a^{-1} at depths of greater than some tens of meters and approaching the modeled value of 0.002 a^{-1} below ~60 m. The results are consistent with CCM-derived strain rates and submergence velocities.

The DIR is relatively thin (~550 m) and subject to relatively high surface accumulation (~0.52 m ice equivalent a^{-1}), which combine with the Raymond effect (Raymond et al., 1983) to dictate vertical strain and velocity at this location (Lingle and Troshina, 1998; Matsuoka et al., 2015). Our OPTV-derived strain rates show notable high-resolution variability with depth, which cannot be reconstructed from ice-flow models. Such variability is likely related to temporal changes in SMB and ice thermo-physics as well as high-resolution variations in material compressibility. The OPTV-based layer differencing method presented herein could be used to investigate such effects, in particular that of, for example, infiltration ice layers on ice firnification and deformation.

The strain rates reported herein combine firn densification and lateral ice deformation. We isolated these contributions using the available density profile and compared the resulting ice equivalent strain rates with output from a full-Stokes model. The model under-estimates strain rate variability over the whole profile (e.g. larger strain values in the first 10 m and in the depth interval 24-45 m). One explanation for this might lie in the model's inability to incorporate temporally-variable surface accumulation and hence associated strain rate. Instead, these values are fixed in the model at their long-term average rates. Indeed, an increase in accumulation over recent decades, as indicated by analysis of the IC12 ice core (Philippe et al., 2016), would have the effect of increasing the modelled vertical strain near the surface, bringing the model output into closer agreement with our measured profile. However, we refrain from further interpretation as the regularized strain rates are less reliable close to the boundaries, particularly shallower than a depth of 10 m where measurements are scarce. Discarding the shallowest data point reduces the variability from 5 10^{-3} to 8 10^{-4} a^{-1}. Strain-rate variability at any smaller scale is difficult to interpret due to insufficiently high resolution or tightly constrained density data. Importantly, OPTV luminosity traces can be used to reconstruct material density (Hubbard et al., 2013). However, slight layer blurring and centimetric-scale uncertainty in logging depth have to date precluded OPTV-based density reconstruction at scales finer than ~0.1 m. Nonetheless, should finer resolution equivalence be demonstrated, then OPTV logs could provide vertical strain and density data at a similar millimetric resolution.

Vertical velocities can be used to reconstruct initial (surface) annual layer thicknesses from measured annual layer thicknesses (as those measured for IC12 by Philippe et al., 2016) which can then be converted to SMB, knowing the surface snow density and assuming that the vertical velocity profile has not changed since layer deposition (i.e., the velocity field is in steady-state). Therefore, the OPTV-based layer differencing method presented herein can provide a means of reconstructing SMB more accurately than any model and without the need for a density profile (Schwerzmann et al., 2006). The age-depth relationship can also be deduced directly from the vertical velocity profile (e.g., Hawley et al., 2002), to improve model-based ice core chronologies and provide useful validation for ice-core dating when annual layering is not clear. The comparison of such chronologies can then highlight deviations from the steady-state condition.

Future work should assess the potential of this technique for strain rate measurements in boreholes drilled by hot water. If the patterns are still clearly identifiable, rapid access to multiple boreholes would allow the measurements to be extended spatially and/or vertically, by drilling to the bedrock. This also cancels the need for digging an access trench and reduces uncertainties associated with a moving surface reference.

3.3.1.5 Acknowledgments and Data

This paper forms a contribution to the Belgian Research Programme on the Antarctic (Belgian Federal Science Policy Office), Project SD/SA/06A Constraining ice mass changes in Antarctica (IceCon). The authors wish to thank the International Polar Foundation for logistic support in the field. MP is partly funded by a grant from Fonds David et Alice Van Buuren. The authors thank Sophie Berger for compiling Figure 3.3.1.1 (location map). The CCM data and OPTV logs presented herein can be accessed in PANGAEA (insert doi).

3.3.1.6 References

Altamimi Z, P. Sillard, C. Boucher (2007), CATREF software: Combination and analysis of terrestrial reference frames. LAREG Technical, Institut Géographique National, Paris, France

Altamimi, Z., P. Rebischung, L. Métivier, and C. Xavier (2016), ITRF2014: A new release of the International Terrestrial Reference Frame modeling nonlinear station motions, J. Geophys. Res. Solid Earth, 121, 6109–6131, doi:10.1002/2016JB013098

Arthern, R. J., Vaughan, D. G., Rankin, A. M., Mulvaney, R., and Thomas, E. R. (2010), In situ measurements of Antarctic snow compaction compared with predictions of models, J. Geophys. Res., 115, F03011, doi:10.1029/2009JF001306.

Berger, Sophie, Lionel Favier, Reinhard Drews, Jean Jacques Derwael, and Frank Pattyn. 2016. “The Control of an Uncharted Pinning Point on the Flow of an Antarctic Ice Shelf.” Journal of Glaciology 62 (231). Cambridge University Press: 37–45. doi:10.1017/jog.2016.7.

Chartrand, R. (2011), International Scholarly Research Network ISRN Applied Mathematics, 164564, doi:10.5402/2011/164564

Dach R., F. Andritsch, D. Arnold, S. Bertone, P. Fridez, A. Jäggi,Y. Jean, A. Maier, L. Mervart, U. Meyer, E. Orliac, E. Ortiz–Geist, L. Prange, S. Scaramuzza, S. Schaer, D. Sidorov, A. Sušnik, A. Villiger, P. Walser, C. Baumann, G. Beutler, H. Bock, A. Gäde, S. Lutz, M. Meindl, L. Ostini, K. Sośnica, A. Steinbach, D. Thaller (2015), Bernese GNNS Software Version 5.2, Eds. R. Dach, S. Lutz, P. Walser and P. Fridez, Astron. Inst. University of Bern, Switzerland

Dansgaard, W. and Johnsen, S. (1969), A flow model and a time scale for the ice core from Camp Century, Greenland, J. Glaciol., 8, 215–223.

Davis, C. H., Y. Li, J. R. McConnell, M. M. Frey, and E. Hanna (2005), Snowfall-Driven Growth in East Antarctic Ice Sheet Mitigates Recent Sea-Level Rise, Science, 308(5730), 1898-1901.

Depoorter, M A, J L Bamber, J a Griggs, J T M Lenaerts, S R M Ligtenberg, M R van den Broeke, and G Moholdt. 2013. “Calving Fluxes and Basal Melt Rates of Antarctic Ice Shelves.” Nature 502 (7469). Nature Publishing Group: 89–92. doi:10.1038/nature12567.

Dow, J.M., Neilan, R.E. & Rizos, C. (2009), The International GNSS Service in a changing landscape of Global Navigation Satellite Systems, J Geod 83: 191. doi:10.1007/s00190-008-0300-3

Drews, R., Matsuoka, K., Martín, C., Callens, D., Bergeot, N., and Pattyn, F. (2015), Evolution of Derwael Ice Rise in Dronning Maud Land, Antarctica, over the last millennia. Journal of Geophysical Research: Earth Surface, 120(3), 564–579.

Gillet-Chaulet, F., Hindmarsh, R. C., Corr, H. F., King, E. C., & Jenkins, A. (2011). In-situquantification of ice rheology and direct measurement of the Raymond Effect at Summit, Greenland using a phase-sensitive radar. Geophysical Research Letters, 38(24).

Hamilton, G. S., and Whillans, I. M. (2000). Point measurements of mass balance of the Greenland ice sheet using precision vertical global positioning system (GPS) surveys. J. Geophys. Res.: Solid Earth, 105(B7), 16295-16301.

Hamilton, G.S., I.M. Whillans and P.J. Morgan (1998), First point measurements of ice sheet thickness change in Antarctica. Ann. Glaciol., v.27, 125-129.

Hawley, R. L. and Waddington, E. D. (2011), In situ measurements of firn compaction profiles using borehole optical stratigraphy, J. Glaciol., Vol. 57, No. 202.

Hawley, R. L., Waddington, E. D., Morse, D. L., Dunbar, N. W., & Zielinski, G. (2002), Dating firn cores by vertical strain measurements. J. Glaciol., 48(162), 401-406.

Hubbard, B., Roberson, S., Samyn, D., and Merton-Lyn, D. (2008), Digital optical televiewing of ice boreholes. J. Glaciol., 54(188), 823-830.

Hubbard, B., Tison, J. L., Pattyn, F., Dierckx, M., Boereboom, T., and Samyn, D. (2012), Optical-televiewer-based identification and characterization of material facies associated with an Antarctic ice-shelf rift, Ann. Glaciol., 53(60), 137-146.

Hubbard, B., and Malone, T. (2013), Optical-televiewer-based logging of the uppermost 630 m of the NEEM deep ice borehole, Greenland, Ann. Glaciol., 54(64), 83-89.

Hubbard, B., J.-L.Tison, M. Philippe, B. Heene, F. Pattyn, T. Malone and J. J. Freitag, (2013b). Ice shelf density reconstructed from optical televiewer borehole logging. Geophys. Res. Lett., 40(22): 5882-5887.

Hubbard, B., Luckman, A., Ashmore, D. W., Bevan, S., Kulessa, B., Kuipers, M. Philippe, D. Jansen, A. Booth, H. Sevestre, J. L. Tison, M. O’Leary, and I. Rutt (2016), Massive subsurface ice formed by refreezing of ice-shelf melt ponds, Nat. Comm., 7, 11897.

Jezek, K, and RAMP-Product-Team (2002), “RAMP AMM-1 SAR Image Mosaic of Antarctica.” Fairbanks, AK: Alaska Satellite Facility, in Association with the National Snow and Ice Data Center, Boulder, CO. Digital Media.

Kingslake, J., R. C. A. Hindmarsh, G. Aðalgeirsdóttir, H. Conway, H. F. J. Corr, F. Gillet-Chaulet, C. Martín, E. C. King, R. Mulvaney, and H. D. Pritchard: Full-depth englacial vertical ice sheet velocities measured using phase-sensitive radar, J. Geophys. Res.: Earth Surface, 119(12), 2604-2618, 2014.

Kingslake, J., C. Martín, R. J. Arthern, H. F. J.Corr, and E. C. King (2016), Ice-flow reorganization in West Antarctica 2.5 kyr ago dated using radar-derived englacial flow velocities, Geophys. Res. Lett., 43, doi:10.1002/2016GL070278.

Lenaerts, J. T. M., S. Lhermitte, R. Drews, S. R. M. Ligtenberg, S. Berger, V. Helm, C. J. P. P. Smeets, et al. 2017. “Meltwater Produced by Wind–albedo Interaction Stored in an East Antarctic Ice Shelf.” Nat. Clim. Change 7 (1). Nature Research: 58–62. doi:10.1038/nclimate3180.

Lingle, C. S., & Troshina, E. N. (1998), Relative magnitudes of shear and longitudinal strain rates in the inland Antarctic ice sheet, and response to increasing accumulation. Ann. Glaciol., 27(1), 187-193.

Malone, T., B. Hubbard, D. Merton-Lyn, P. Worthington & R. Zwiggelaar (2013), Borehole and Ice Feature Annotation Tool (BIFAT): A program for the automatic and manual annotation of glacier borehole images. Computers & Geosciences, 51, 381-389.

Martín, C., Mulvaney, R., Gudmundsson, G. H., & Corr, H. (2015). Inferring palaeo-accumulation records from ice-core data by an adjoint-based method: application to James Ross Island's ice core. Clim. Past, 11(3), 547-557.

Matsuoka, K., Hindmarsh, R. C., Moholdt, G., Bentley, M. J., Pritchard, H. D., Brown, J., Conway, H., Drews, R., Durand, G., Goldberg, D., Hattermann, T., Kingslake, J., Lenearts, J., Martin, C., Mulvaney, R., Nicholls, K., Pattyn, F., Ross, N., Scambos, T., and Whitehouse, P. (2015) Antarctic ice rises and rumples: their properties and significance for ice-sheet dynamics and evolution. Earth-Sci. Rev., 150, 724–745, doi: 10.1016/j.earscirev.2015.09.004, 20

Nicholls, K. W., Corr, H. F., Stewart, C. L., Lok, L. B., Brennan, P. V., & Vaughan, D. G. (2015). A ground-based radar for measuring vertical strain rates and time-varying basal melt rates in ice sheets and shelves. J. Glaciol., 61(230), 1079-1087.

Nye, J.F.: Correction factor for accumulation measured by the thickness of the annual layers in an ice sheet. J. Glaciol., 4(36), 785-788, 1963.

Philippe, M., Tison, J.-L., Fjøsne, K., Hubbard, B., Kjær, H. A., Lenaerts, J. T. M., Drews, R., Sheldon, S. G., De Bondt, K., Claeys, P., and Pattyn, F. (2016). Ice core evidence for a 20th century increase in surface mass balance in coastal Dronning Maud Land, East Antarctica, The Cryosphere, 10, 2501-2516, doi:10.5194/tc-10-2501-2016.

Raymond, C., Weertman, B., Thompson, L., Mosley-Thompson, E., Peel, D., and Mulvaney, R.: Geometry, motion and balance of Dyer Plateau, Antarctica, J. Glaciol., 42, 510–518, 1996.

Schwerzmann, A., Funk, M., Blatter, H., Lüthi, M., Schwikowski, M. and Palmer, A.: A method to reconstruct past accumulation rates in alpine firn regions: A study on Fiescherhorn, Swiss Alps, Mitteilungen der Versuchsanstalt fur Wasserbau, Hydrol. und Glaziologie an der Eidgenoss. Tech. Hochschule Zurich, 111(194), 53–66, doi:10.1029/2005JF000283, 2006.

Spikes, V. B., Csathó, B. M., Hamilton, G. S., & Whillans, I. M. (2003). Thickness changes on Whillans Ice Stream and Ice Stream C, West Antarctica, derived from laser altimeter measurements. Journal of Glaciology, 49(165), 223-230.

Thomas, E. R., G. J. Marshall, and J. R. McConnell (2008), A doubling in snow accumulation in the western Antarctic Peninsula since 1850, Geophys. Res. Lett., 35, L01706, doi: 10.1029/2007GL032529

Raymond, C. F. (1983), Deformation in the vicinity of ice divides, J. Glaciol., 29(103), 357–373.

3.3.2 Implications for SMB corrections

We presented the importance of SMB measurements from ice cores and the need to account for densification and ice flow, when correcting annual layer thicknesses. In the vast majority of SMB studies, these corrections can only be made with a density profile for the former and an ice flow model for the latter (e.g. Sect. 3.2).

Here, we use the method described in Schwerzmann et al. (2006) to correct annual layer thickness using only the vertical velocity profile calculated in Sect. 3.3.1. Interestingly, this method does not require the knowledge of the density profile but rather requires assumptions on the steady state of this density profile, of vertical velocity fields and of surface elevation. We apply one of the two equivalent methods described in Schwerzmann et al. (2006), where the initial layer thickness h_A of snow deposited during one year at the surface is reconstructed from the observed layer thickness h_B at a given depth z_B, multiplied by a correction factor.

Using equation 3.3.1.1 ($w(z)= dz/dt$), and assuming that $w(z)$ is in steady state, it follows that $\Delta z = w(z)\ \Delta t$. Therefore, for the same annual layer, its initial thickness at the surface is given by $h_A = w_A\ \Delta t$ and, at depth z_B, the observed thickness of the layer is given by $h_B = w_B\ \Delta t$. Therefore, the correction factor ($k_A= h_A / h_B$) is the ratio of vertical velocities at the surface w_A and at depth z_B, w_B. The initial water equivalent annual layer thickness is then obtained by multiplying $h_B\ w_A / w_B$ by the mean density of annual snow layers deposited at the ice surface ρ_A divided by the density of water ρ_w as in Eq. 3.3.2 (Eq. 5 in Schwerzmann et al., 2006)

$$h_A^{w.e.} = h_B \frac{\rho_A w_A}{\rho_w w_B} \qquad \text{Eq. 3.3.2}$$

Therefore, we do not need the whole density profile but only the density of the top annual snow layer.

We apply this correction to our annual layer thicknesses measured in Sect. 3.2, using the vertical velocity profile calculated from repeat borehole OPTV and GNSS, described in Section 3.3.1. From now on we refer to this simply by “SMB correction from OPTV”, which we compare to “SMB corrected from model” presented in Sect. 3.2. For the SMB correction from OPTV, errors are calculated from standard propagation of: (i) 5 cm errors on observed annual layer thickness h_B, due to the resolution of the chemical analyses, (ii) 8.5 mm errors on surface velocity measured with GNSS w_A, and (iii) an arbitrary 25 kg m^{-3} error on the density of an annual snow layer deposited at the surface (ρ_A) to account for the 4% error on the density profile (estimated in Sect. 3.1) and the variable thickness of this snow layer. Indeed, we use the mean density of a surface snow layer of ~1 m, which corresponds to the mean h_A reconstructed for the whole core (in real thickness, not w.e.). This thickness has a standard deviation of 0.4 m, which translates into an additional error on the mean density of that surface snow layer (as density increases exponentially with depth, a thicker surface snow layer will have a higher mean density than a thinner surface snow layer). This additional error on ρ_A is not taken into account in Schwerzmann et al. (2006). We also take into account the directional (5 cm compaction) error on relative velocity described in Sect. 3.3.

Table 3.3.1. Comparison between corrections from model (Sect. 3.2) and from OPTV (this section) for revised SMB estimates reported in Table 3.2.1 (note that 1816 was replaced by 1848 since OPTV corrections could not be made below 100 m). Numbers, errors and uncertainty ranges are averaged between oldest and youngest estimates (see text for details).

Period (years AD)	SMB corrected from model (m w.e. a^{-1})	SMB corrected from OPTV (m w.e. a^{-1})
1848–2011	0.51 ± 0.056	0.49 [0.41 to 0.6]
1848–1961	0.47 ± 0.056	0.43 [0.36 to 0.54]
1962–2011	0.6 ± 0.056	0.63 [0.55 to 0.74]
1848–1991	0.49 ± 0.057	0.47 [0.39 to 0.58]
1992–2011	0.61 ± 0.053	0.66 [0.58 to 0.76]
1848–1900	0.43 ± 0.055	0.37 [0.3 to 0.48]
1900–2011	0.54 ± 0.057	0.55 [0.47 to 0.66]

Results are shown in Table 3.3.1 and Fig. 3.3.2. For clarity, we only show averages between oldest and youngest estimates and average error bars between both estimates. In Table 3.3.1, SMB corrections from OPTV are expressed with uncertainty ranges, because of the directional error mentioned previously, while SMB corrections from the full-Stokes model are expressed with symmetrical error bars. The latter errors are smaller than the former, because we have not estimated errors on the modelled strain rates and vertical velocities. As shown in Fig. 3.3.2c, visual comparison of SMB corrections from OPTV to SMB corrections from the full-Stokes model indicates that the former stay within the error bars of the latter, giving confidence in our previous analyses. However, SMB corrected from OPTV in the oldest part of the record matches the lower bound of these error bars, while SMB in the youngest part matches their upper bound. Therefore, if the method and its assumptions are valid, the model underestimated the rate of increase of SMB throughout the observational period and Sect. 3.2 should be revised in the following way (strikethrough italic numbers between parentheses refer to previous percentages of change estimated from the model in section 3.2):

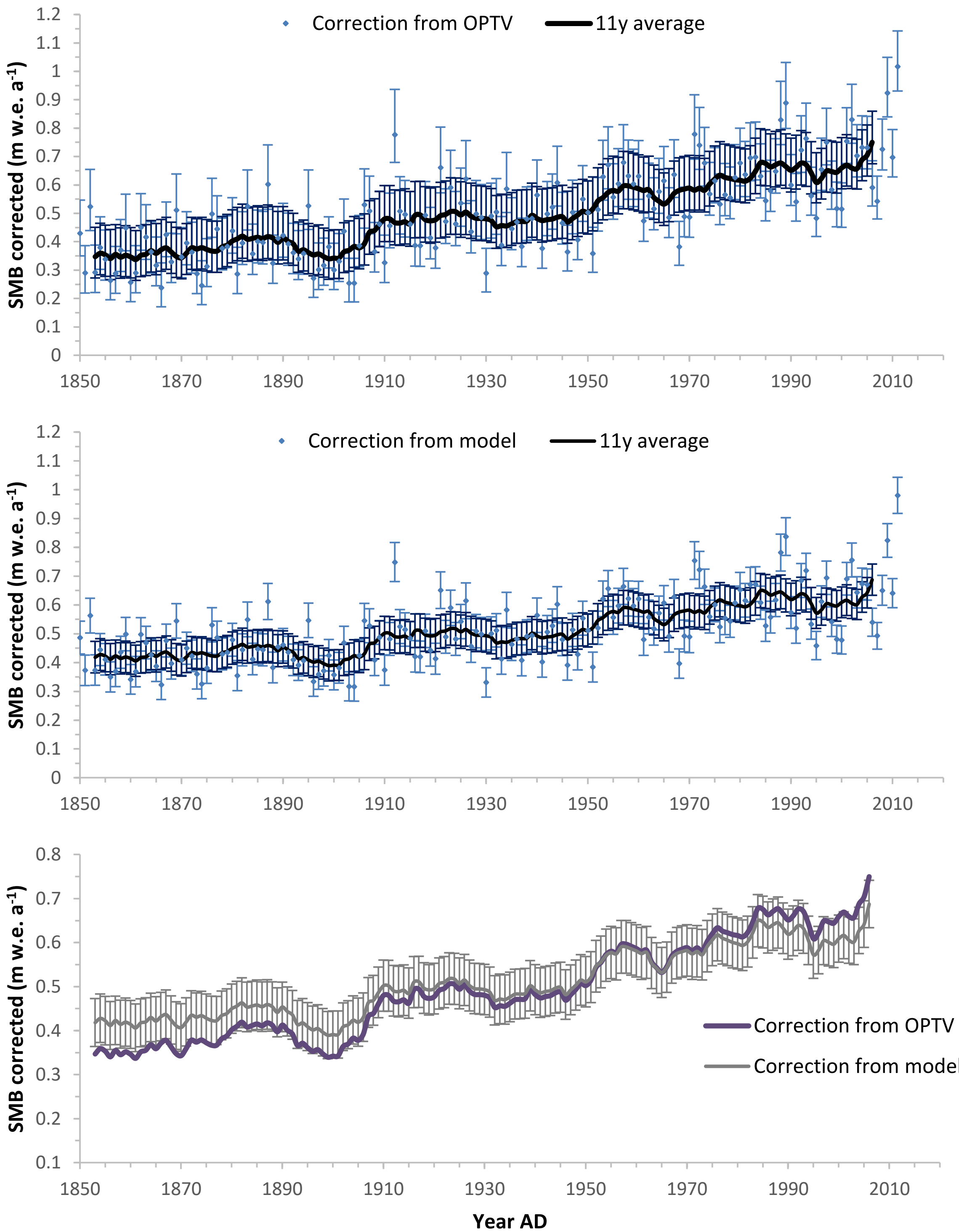

Figure 3.3.2. Corrections from (a) OPTV (this section) and (b) the full-Stokes model (Sect. 3.2) and for revised annual and 11 y averaged SMB estimates reported in Fig. 3.2.6. Panel (c) compares 11y averaged SMB corrections from OPTV to 11 y averaged SMB corrections from model and associated error bars. For clarity, only averages between oldest and youngest estimates are shown and error bars reflect associated uncertainties (see text for details).

For the full 163-year time period (1848–2011), the mean SMB, including correction for layer thinning, is 0.49 [0.41 to 0.6] m w.e. a^{-1}. For the last 111 years (1900–2011), the SMB is 0.55 [0.47 to 0.66] m w.e. a^{-1}

representing a 36 [30 to 42] % increase compared to the previous period (1848–1900). For the last 50 years (1962–2011), the SMB is 0.63 [0.55 to 0.74] m w.e. a^{-1}, representing a 38 [30 to 46] % increase compared to the previous period (1848–1962). For the last 20 years (1992–2011), the SMB is 0.66 [0.58 to 0.76] m w.e. a^{-1}, representing a 40 [33 to 48] % increase compared to the previous period (1848–1992).

Most importantly, all the conclusions and interpretations from Sect. 3.2 still hold and these new observation-based SMB corrections further demonstrate their validity and interest. However, the increase in SMB starts earlier and is stronger than the increase reported in Sect. 3.2.

It should also be noted that the higher % of each range corresponds to the older estimate, which was suggested as the most probable scenario in section 3.2. Finally, it should be stressed that both approaches (corrections from model and corrections from OPTV) are based on estimates of strain thinning in a steady state approach (i.e. constant density and vertical velocity profile). The observed trend in accumulation rates suggests that the vertical velocity profile might also have changed with time. However, a change in strain regime alone cannot explain the observed increase in w.e. annual layer thicknesses.

The next section will evaluate possible deviation from the steady state hypothesis by comparing age-depth profiles obtained from OPTV-derived velocities with that obtained from the IC12 ice core analysis.

3.3.3 Independent check on the age-depth profile and preliminary implications for the steady-state hypothesis

Age-depth profiles are needed for every climate reconstruction from ice-cores or radar surveys. They allow rapid extraction of long-term SMB.

The method presented in Sect. 3.2 is based on annual layer counting in the IC12 ice core to extract a "geochemical age" (measured on the basis of chemical analyses). Here we calculate a "geophysical age" (we adopt the terminology used in Hawley et al. (2002) to refer to the theoretical age-depth scale developed in this section without annual layer counting) using the vertical velocities measured in Sect. 3.3.1. and assuming a steady state vertical velocity profile. Geophysical age-depth profiles are useful when annual layering is not available or not clear, or to compare different dating methods.

Comparing geochemical and geophysical ages provides information on variation in accumulation rate (deviation from steady state). As Sect. 3.2 concluded a recent increase in accumulation rates (SMB) and therefore in vertical velocity (Cuffey and Paterson, 2010, p.13), we expect that the geochemical age will exceed the geophysical age.

We numerically integrate the inverse of the submergence velocity from the surface to depth z to find the age at depth z (Paterson et al., 1977; Hawley et al., 2002)

$$w(z) = \frac{dz}{dt} \qquad \text{Eq. 3.3.3.1}$$

$$age = \int_0^z \frac{1}{w(z)} dz \qquad \text{Eq. 3.3.3.2}$$

Figure 3.3.3 shows the age-depth profile from the IC12 ice core analysis with the associated uncertainty resulting from our oldest and youngest estimates, presented in Sect. 3.2. This is compared with the age-depth profile reconstructed from OPTV-measured vertical velocity combined with the surface velocity (-1.38 ± 0.009 m a^{-1}) measured using GNSS measurements through 2013 and 2014.

In Fig. 3.3.3, the top part (0-~50 m) of the profile indicates a geochemical age consistent with the geophysical age (~55 years BP at 50 m). Below that depth, the geochemical age profile exceeds the geophysical age with discrepancies increasing with depth. At 100 m, the mean geochemical age is 176 ± 11 years BP, while the geophysical age is 127 [118 to 129] years BP.

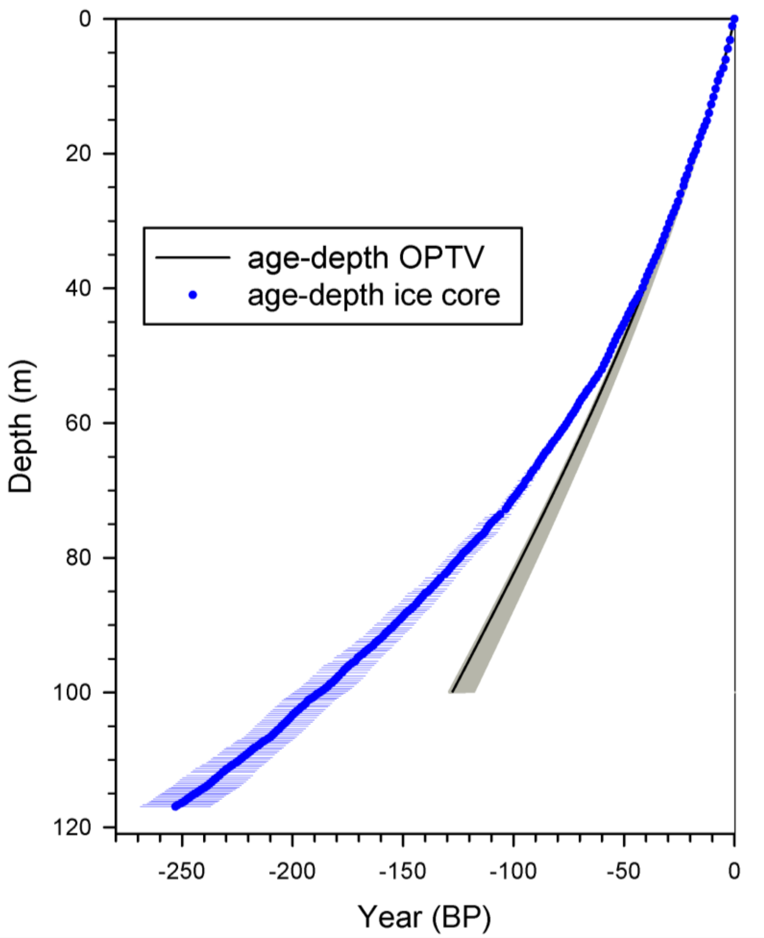

Figure 3.3.3. "Geophysical age" depth profile (black line, from vertical velocity measured using repeat OPTV borehole logging combined with GNSS-measured surface velocities) with associated error range (grey shading), see details in Sects. 3.3.1 and 3.3.2. "Geochemical age" depth profile, measured from ice-core annual layer counting (blue dots) with associated uncertainty range, see details in Sect. 3.2. BP : before present (2012)

These results cross-validate the dating and the submergence velocity measurements in the uppermost ~50 m of IC12. However, they also indicate an increasing offset between the geochemical age and the geophysical age below that depth. This increasing offset is due to the fact that the geophysical age is reconstructed using present-day surface velocity. These results indicate a higher submergence velocity in the recent past (last ~55 years)., which is consistent with a recent increase in SMB.

The precise impact of this deviation from the steady-state hypothesis on SMB corrections made in Sect. 3.3.2 could be assessed by incorporating variable accumulation rates in an ice-flow model to match the observed age-depth profile (Waddington et al., 2005), but this is beyond the scope of this thesis.

4 CONTRIBUTION TO OTHER STUDIES

Full versions of the papers summarized in this section can be found at the end of the Appendix.

4.1 Surface Mass Balance of Antarctic ice rises

4.1.1 Temporally stable surface mass balance asymmetry across an ice rise derived from radar internal reflection horizons through inverse modeling

This section is a summary of Callens et al. (2016) where all references are mentioned.

Paper published in Journal of Glaciology, 62 (233), June 2016, pp. 525-534, doi:10.1017/jog.2016.41

Title: Temporally stable surface mass balance asymmetry across an ice rise derived from radar internal reflection horizons through inverse modeling

Authors: Denis Callens[1], Reinhard Drews[1], Emmanuel Witrant[1,2], Morgane Philippe[1], Frank Pattyn[1]

[1]Laboratoire de Glaciologie, Université Libre de Bruxelles, Avenue F.D. Roosevelt 50, B-1050, Bruxelles, Belgium
[2]GIPSA-lab, Université Grenoble Alpes, F-38000, Grenoble, France

Correspondence to: Reinhard Drews (rdrews@ulb.ac.be)

Abstract: Ice rises are locally grounded parts of Antarctic ice shelves that play an important role in regulating ice flow from the continent towards the ocean. Because they protrude out of the otherwise horizontal ice shelves, ice rises induce an orographic uplift of the atmospheric flow, resulting in an asymmetric distribution of the surface mass balance (SMB). Here, we combine younger and older internal reflection horizons (IRHs) from radar to quantify this distribution in time and space across Derwael Ice Rise (DIR), Dronning Maud Land, Antarctica. We employ two methods depending on the age of the IRHs, i.e. the shallow layer approximation for the younger IRHs near the surface and an optimization technique based on an ice flow model for the older IRHs. We identify an SMB ratio of 2.5 between the flanks and the ice divide with the SMB ranging between 300 and 750 kg m^{-2} a^{-1}. The SMB maximum is located on the upwind side, ~4 km offset to today's topographic divide. The large-scale asymmetry is consistently observed in time until 1966. The SMB from older IRHs is less-well constrained, but the asymmetry has likely persisted for >ka, indicating that DIR has been a stable feature over long time spans.

Keywords: Antarctic glaciology, ground-penetrating radar, ice rise, ice-sheet modelling, surface mass budget

Ice rises induce an SMB asymmetry due to an orographic uplift of the moist air coming from the ocean towards the coast (Lenaerts et al., 2014; Sect 4.1.2). The aim of Callens et al. (2016) was to quantify this asymmetry spatially and temporally across the DIR. They used ground penetrating radar to map internal reflection horizons (IRHs) along a 32 km profile (Fig. 4.1). They identified a set of shallower, younger IRHs (1966-2012) and another set of deeper, older IRHs, with high frequency (400 MHz) and low frequency radar (2 MHz), respectively (Fig. 4.2). The spatial pattern in the IRH reflects the spatial variability of SMB on the different time periods bounded by the selected IRHs. To date the younger IRHs, they used the age-

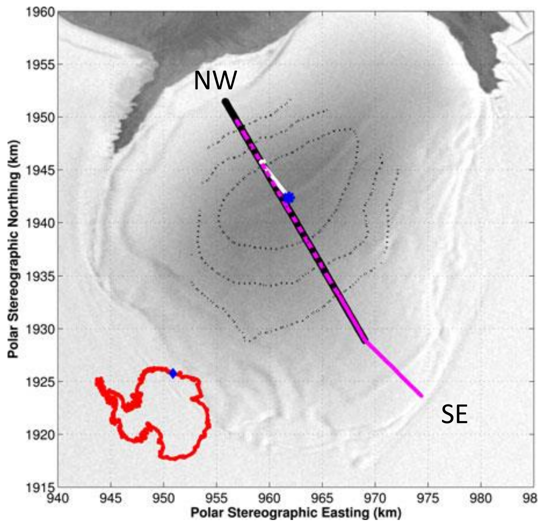

Figure 4.1. (left) Map of DIR. The thick black line is the 2 MHz profile. The dashed and solid purple lines are the 400 MHz profiles of 2012 and 2013, respectively. The white line is the link to the borehole (blue star). The core site is located at the divide. Radarsat is used as a background image (Jezek and RAMP-Product-Team, 2002)*. The dotted lines are contours of 300, 350 and 400 m a.s.l. The inset in the bottom left corner depicts the location of DIR in Antarctica. NW and SE refer to north-western and south-eastern ends of the profile, respectively (Callens et al., 2016)*

Figure 4.2 (bottom) GPR profile along Derwael Ice Rise. Note that the transect runs from the upwind slope (SE) to the downwind slope (NW), but is presented from NW to SE in Figs 4.3 and 4.4. The red curve denotes the selected reflector for the SMB estimation in Sect. 4.1.2. The dashed black line is the position of the ridge and the IC12 core. The blue line denotes the separation between the data obtained in 2012 and in 2013 (Figure 2 in Lenaerts et al., 2016).

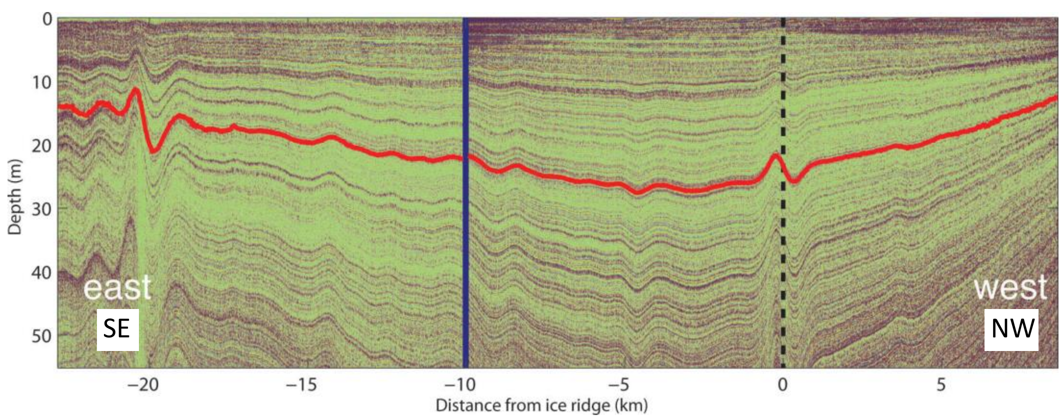

depth relationship given by the ice core (Sect. 3.2) and for the older IRHs, they used an age-depth relationship computed from a simple ice flow model (Nye, 1963), avoiding the central part of the profile where the Raymond effect limits its validity. As the wave propagation into ice depends on its density, a density model from Arthern et al. (2010) was used to calibrate radar depths.

The work presented in this thesis contributed to that research in different ways. The vertical profiles of temperature and density (Sect. 3.1) were used to parametrize the density model. The age-depth relationship from the core allowed the dating of 5 younger IRHs selected between the surface and a depth of 44 m (Fig. 4.3b). Finally, our SMB estimate (Sect. 3.2) was fed as an input to the model that aimed at dating the older IRHs.

The main results are summarized in Fig 4.4. The spatial asymmetry in SMB is visible and consistent at all depths with SMB values ranging between 300 kg m^{-2} a^{-1} and 750 kg m^{-2} a^{-1} (ratio of 2.5). This involves that the conditions leading to this spatial pattern have been constant on the DIR, at least since 1966.

The SMB given by the older IRHs is less constrained, as it requires assumption on long term SMB at the divide. A sensitivity analysis showed that a 10 % older age-depth relationship would give a better fit to the observed IRHs, which we relate to the recent increase in SMB described in Sect. 3.2.

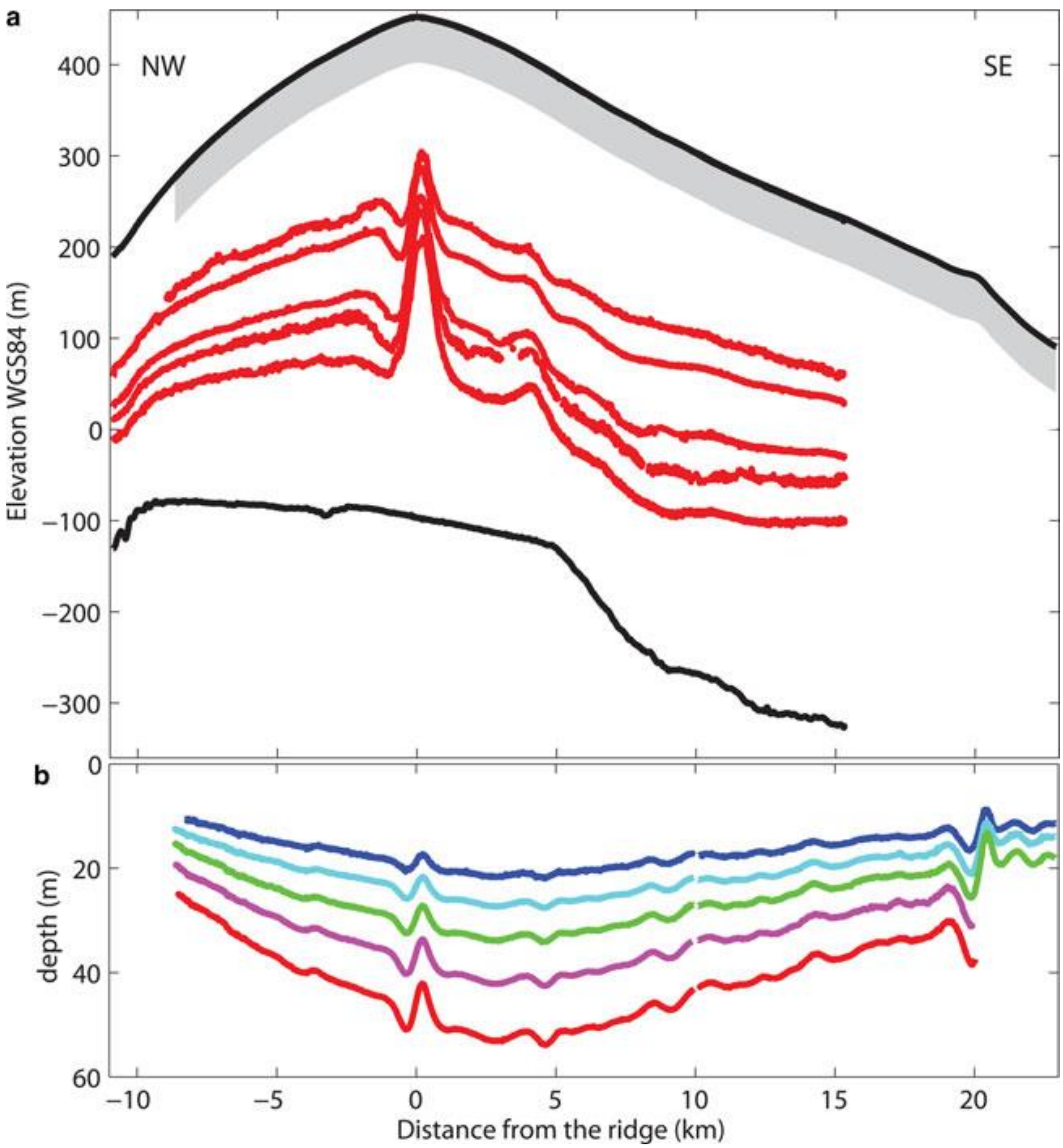

Figure 4.3 (a) Geometry of DIR. Bed and surface are in black and older IRHs detected with the 2 MHz radar are marked in red. The grey zone is the detection range of the 400 MHz radar. (b) Depth of the younger IRHs located in the grey zone of panel (a). The small data gap situated around +10 km is the link between data from 2012 and 2013 (Figure 2 in Callens et al., 2016).

The spatial SMB pattern from the older IRHs is overall similar to the SMB patterns from the younger IRHs, which indicates that the DIR has probably been stable for thousands of years, which is consistent with the Raymond arches observed below its divide (Drews et al., 2015).

It is interesting to compare the temporal variability in SMB between the method presented in this section and the ice-core analysis presented in Sect. 3.2. Following Callens et al. (2016), the mean SMB should be between 656 ± 66 kg m^{-2} a^{-1} at the divide for the period 1966-2012 ("ridge" in Fig. 4.4). Our data indicate

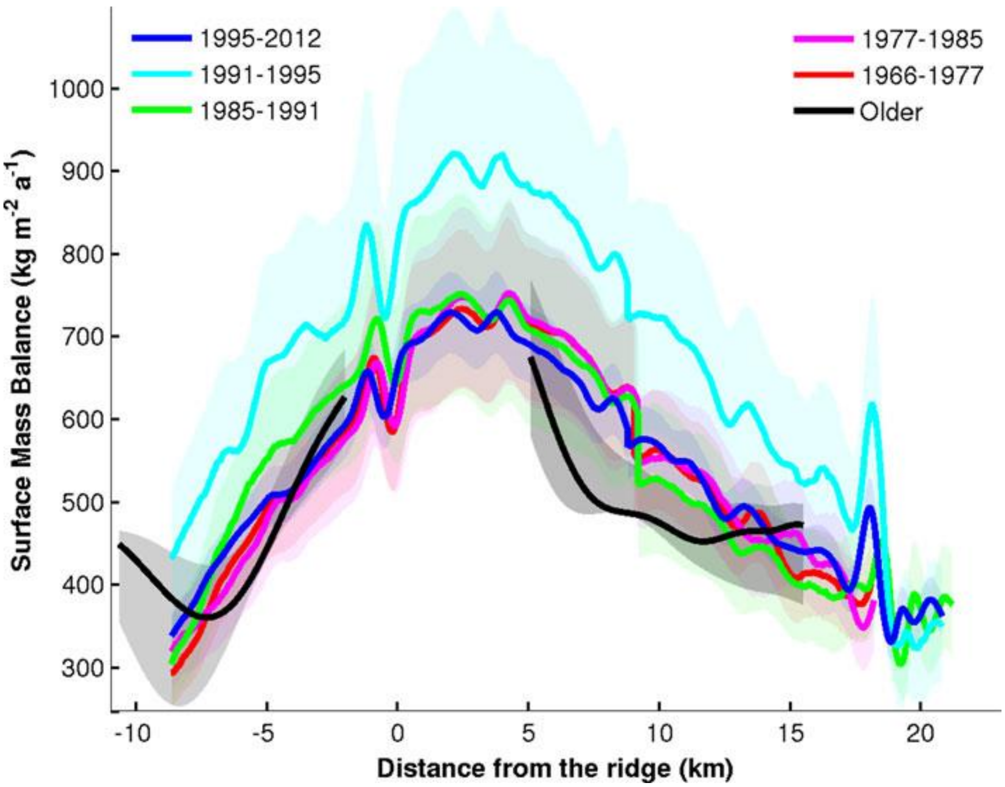

Figure 4.4 Spatial distribution of the SMB across the DIR inferred from younger and deeper IRHs. The shaded areas denote the SMB uncertainties. The solid black curve is the result of the optimization on all older IRHs. The grey shaded area represents the range of SMB derived while taking into account the depth uncertainty of the older IRHs (Figure 3 in Callens et al. (2016)).

that SMB is lower, within the error bar, with a mean of 599 kg m^{-2} a^{-1} (0.599 m w.e. a^{-1}) and a standard deviation of 152 kg m^{-2} a^{-1} (0.152 m w.e. a^{-1}, Fig. 4.5). The 1991-1995 period that appears as a high outlier (710 kg m^{-2} a^{-1}) in Callens et al. (2016) has a mean SMB of 572 kg m^{-2} a^{-1} (0.572 m w.e. a^{-1}) in the ice core data, just below the mean for the whole 1966-2012 period. These discrepancies can be explained by the different density models used (Arthern, 2010 model for the GPR data and the best fit described in Sect. 3.1 for the ice core data) and the errors associated with that density (4% relative error, Sect. 3.1) and with

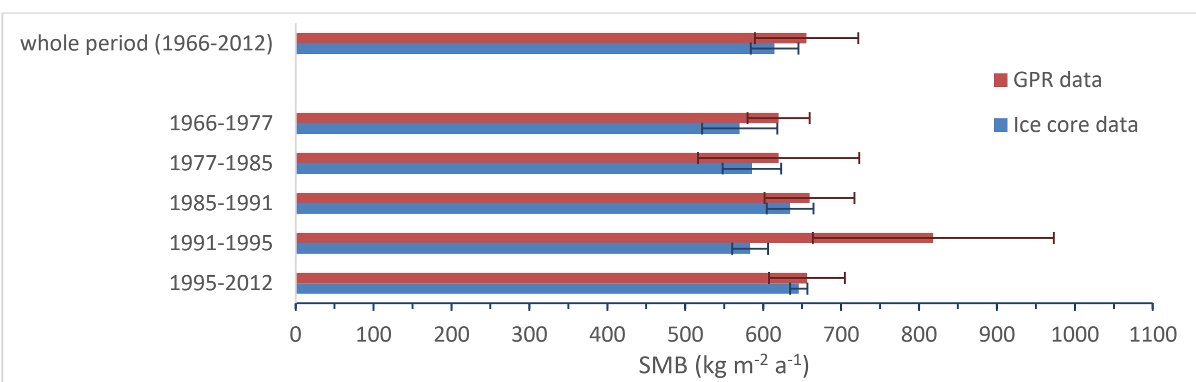

Figure 4.5. SMB data from GPR data at the divide (Callens et al., 2016) and SMB data derived from ice core analysis (Sect. 3.2) and averaged for the corresponding periods. Error bars indicate uncertainty estimates for the GPR method and range between oldest and youngest estimates for ice core data.

SMB averaged over small periods (e.g. 4-12 years). However, SMB for all periods but 1991-1995 remain within the error bars of both methods. The authors also mention that the 1991-1995 outlier is not observed in RACMO2 output. We conclude that the GPR method is convenient to reproduce the spatial SMB pattern but that the temporal variability is not well represented on short time periods.

4.1.2 High variability of climate and surface mass balance induced by Antarctic ice rises

This section is a summary of Lenaerts et al. (2014) where all references are mentioned.

Paper published in Journal of Glaciology, Vol.60, No. 224, 2014, doi: 10.3189/2014JoG14J040

Title: High variability of climate and surface mass balance induced by Antarctic ice rises

Authors: Jan T.M. Lenaerts[1], Joel Brown[2], Michiel R. Van Den Broeke[1], Kenichi Matsuoka[2], Reinhard Drews[3], Denis Callens[3], Morgane Philippe[3], Irina V. Gorodetskaya[4], Erik Van Meijgaard[5], Carleen H. Reijmer[1], Frank Pattyn[3], Nicole P.M. Van Lipzig[4]

[1]Institute for Marine and Atmospheric Research, Utrecht University, Utrecht, The Netherlands
[2]Norsk Polarinstitutt, Tromsø, Norway
[3]Laboratoire de Glaciologie, Université Libre de Bruxelles, Brussels, Belgium
[4]Department of Earth and Environmental Sciences, KU Leuven – University of Leuven, Leuven, Belgium
[5]Royal Netherlands Meteorological Institute, De Bilt, The Netherlands

Correspondence to : Jan Lenaerts (j.lenaerts@uu.nl)

Abstract: Ice rises play key roles in buttressing the neighbouring ice shelves and potentially provide palaeoclimate proxies from ice cores drilled near their divides. Little is known, however, about their influence on local climate and surface mass balance (SMB). Here we combine 12 years (2001–12) of regional atmospheric climate model (RACMO2) output at high horizontal resolution (5.5 km) with recent observations from weather stations, ground-penetrating radar and firn cores in coastal Dronning Maud Land, East Antarctica, to describe climate and SMB variations around ice rises. We demonstrate strong spatial variability of climate and SMB in the vicinity of ice rises, in contrast to flat ice shelves, where they are relatively homogeneous. Despite their higher elevation, ice rises are characterized by higher winter temperatures compared with the flat ice shelf. Ice rises strongly influence SMB patterns, mainly through orographic uplift of moist air on the upwind slopes. Besides precipitation, drifting snow contributes significantly to the ice-rise SMB. The findings reported here may aid in selecting a representative location for ice coring on ice rises, and allow better constraint of local ice-rise as well as regional ice-shelf mass balance.

Keywords: accumulation, Antarctic glaciology, ice rise, surface mass budget, wind-blown snow

The importance of ice rises for ice flow (e.g. Borstad et al., 2013) and for paleoclimate reconstructions (Mulvaney et al., 2007; Bertler et al., 2014; Mulvaney et al., 2014) has been widely documented but their influence on local climate and on SMB spatial variability is less studied. The spatial resolution of SMB maps is too low to resolve local phenomena occurring at a scale of less than 20 km, the usual size of ice rises. This paper used a regional climate model (RACMO2) at a spatial resolution of 5 km to reveal a generic feature in the SMB pattern around ice rise that need to be considered in mass balance inventories, e.g. to determine basal mass balance with a mass-budget approach (Depoorter et al., 2013; Rignot et al., 2013).

SMB is defined as the difference between annual surface mass gain (precipitation, PR) and surface mass loss (surface runoff, RU, surface sublimation, SU_s, drifting snow sublimation, SU_{ds}, and drifting snow erosion (positive) or deposition (negative) ER_{ds}, Eq. 4.1).

$$SMB = \int PR - RU - SU_s - SU_{ds} - ER_{ds} \, dt \qquad \text{Eq. 4.1}$$

The working hypothesis is that ice rises induce an orographic uplift of the air masses, leading to enhanced precipitations on the upwind slope and less precipitations on the downwind slope as the air warms up and dries adiabatically. Snow erosion and associated drifting snow processes are also expected near the crest, due to the disturbance of the local wind field.

To test this hypothesis, the output of the climate model was combined for a 12 years' period, and compared to data from weather stations, ground-penetrating radar and firn cores. The study area is focused on coastal Dronning Maud Land, as this region comprises many small ice rises.

Our contribution was part of a study dedicated to the reconstruction of the SMB spatial and temporal variability from ground penetrating radar (Fig. 4.1) further detailed in Sect. 4.1.1. We provided a vertical profile of temperature and early estimates of the age-depth relationship in the first 40 m and participated to the results interpretation and the paper writing.

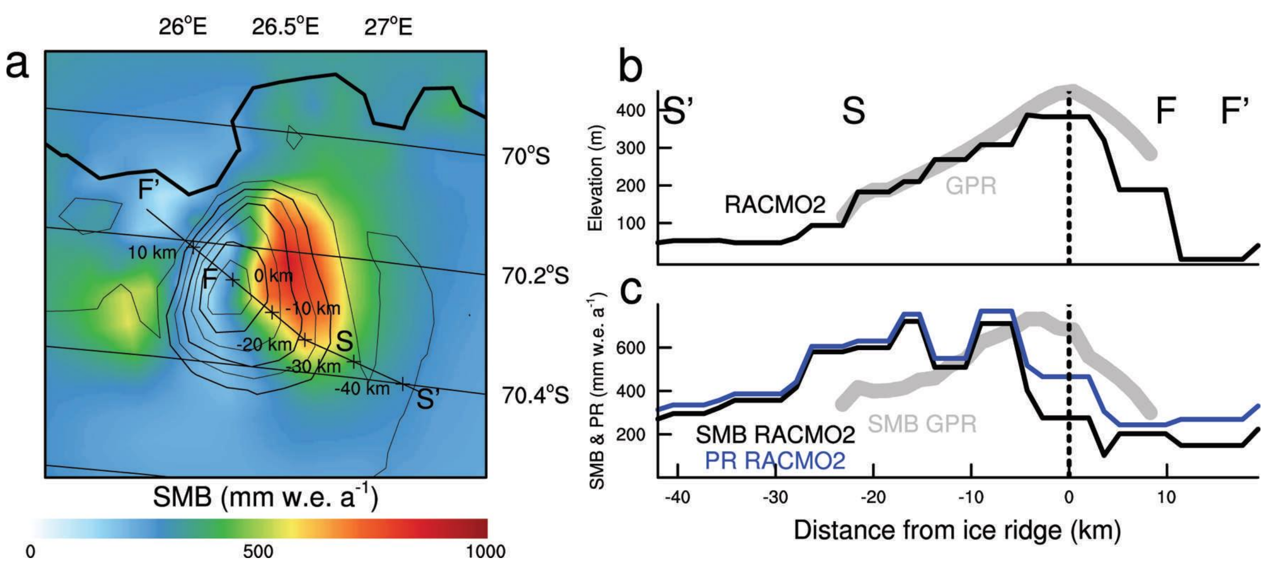

Figure 4.6 (a) RACMO2 mean (2001–12) annual SMB around Derwael Ice Rise and location of transect. (b) Elevation profile and (c) mean SMB along the transect according to RACMO2 (black) and derived from the GPR observations (grey; Fig. 4.2). RACMO2 precipitation, PR, is shown in blue in (c). The vertical dotted line in (b, c) shows the location of the divide. The crosses and numbers in (a) correspond to the distance from the ice ridge, equivalent to the x-axis in (b, c) SMB and elevation are plotted from the upwind slope (S) to the downwind slope (F), i.e. from east to west (Figure 6 in Lenaerts et al., 2016).

The main features of the paper relate to the near-surface temperature of ice rises and the spatial variability of their SMB pattern. The temperature over ice-rises during the winter is higher than the temperature over ice shelves, despite the fact they are at a higher altitude. This is due to the temperature inversion that occurs during the winter on Antarctic ice shelves (Connolley, 1996), and the higher turbulence induced by the topography allowing warmer air to reach down to the surface of the ice rises. The SMB pattern across Derwael ice rise is well reproduced in the regional model, except for small discrepancies (Fig. 4.6, b and c), namely: (i) in the position of the highest SMB, which is attributed to uncertainties in the elevation model, and (ii) in the overall correspondence of the SMB along the radar profile, possibly attributed to variations of surface snow densities or false tracking of the radar reflection horizons.

The prevailing winds in Dronning Maud Land are easterly or southeasterly. However, RACMO2 indicates a precipitation enhanced on the northeastern side of ice rises and a precipitation shadow on the southwestern side (Fig. 4.6a). The model shows that the wind direction during precipitation events, which, in that region, occur mainly in the form of strong episodic events, is from the northeast (Reijmer & Van Den Broeke, 2001; Schlosser et al., 2010; Lenaerts et al., 2013). RACMO2 was also able to reconstruct interannual variability, especially the high SMB that occurred in 2009 and 2011.

The model also confirms the snow erosion and the associated drifting snow processes occurring on the downwind slope of ice rises. The wind field is disturbed at the ice rise ridge and results in the erosion of the snow, which is then deposited further away, on local elevations such as other ice rises or sastrugi, small features made from wind erosion and redistribution (Bromwich et al., 1990). Topographic effects such as horizontal divergence of the wind or strong downslope acceleration and sublimation can also modify SMB very locally. These smaller scale phenomena are not resolved by RACMO2 and can lead to small discrepancies between the model and observations.

To conclude, this analysis shows that the SMB ratio between the downwind slope and the upwind slope ranges between 2 and 6 and is a generic feature of all ice rises. Therefore, mass balance inventories of ice shelves as well as paleoclimate studies should take these prominent features into account.

4.2 Specific features of Antarctic ice shelves

Our contribution to the two papers presented in this section has needed a preliminary assessment of the damages that occurred during the transport of the RBIS14 ice core after the 2014 field season (see Sect. 2.1). Density was measured gravimetrically on 40 discrete samples and was compared to the luminosity, measured by OPTV and converted to density with the same calibration as for IC12 (which was however logged with a different OPTV probe) (Fig. 4.7). Figure 4.7 also shows other density measurements on 5 m firn cores from the same area, collected ~100 m away from RBIS14 (Lenaerts, personal communication). Although the variability in these data (due to the occurrence of icy layers) limits their precise comparison, they confirm the fact that OPTV density is overestimated in the first 10 m, as described in Sect. 3.1.

Above 20 m, only a few RBIS14 core sections could be analyzed gravimetrically, as the other sections showed very clear signs of melting and refreezing during storage. At 5 m depth, RBIS14 densities are lower than the density of the firn cores. They are also lower than OPTV density above 20 m. Below that depth, gravimetric densities and OPTV densities seem consistent. Lower gravimetric density compared to OPTV in the first 20 m could be the result of mass loss in the most porous firn where the meltwater can transfer easily towards the lower part of the core (stored horizontally) and refreeze at the surface of the core. Only the central part of the core was used for the gravimetric measurements. Below 20 m, the permeability of the firn decreases so that the accidental melting of the samples is limited to the surface. Therefore, the central part of these samples could be used for the calibration of the new probe (Fig. 4.8) used in the following studies (Sects 4.2.1 and 4.2.2). The new calibration yields a best-fit regression (R^2=0.82) of Equation 4.2.

$$\rho=950-40.1\, e^{(0.0101\, L)} \quad \text{Eq. 4.2}$$

Where ρ is the density and L is the luminosity.

The associated root mean square values of the residuals are 40.4, 35.2 and 21.7 kg m^{-3} for the density ranges 600–700, 700–800 and 800–900 kg m^{-3}, respectively.

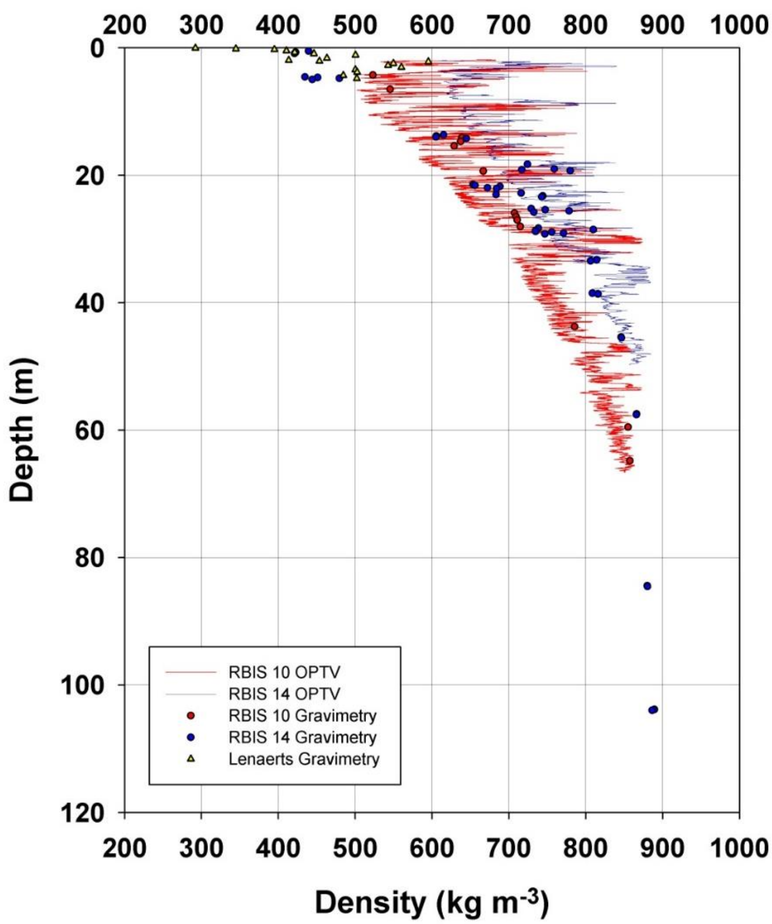

Figure 4.7 Comparison of density profiles from OPTV brightness and gravimetric measurements for the 2010 and 2014 RBIS ice cores

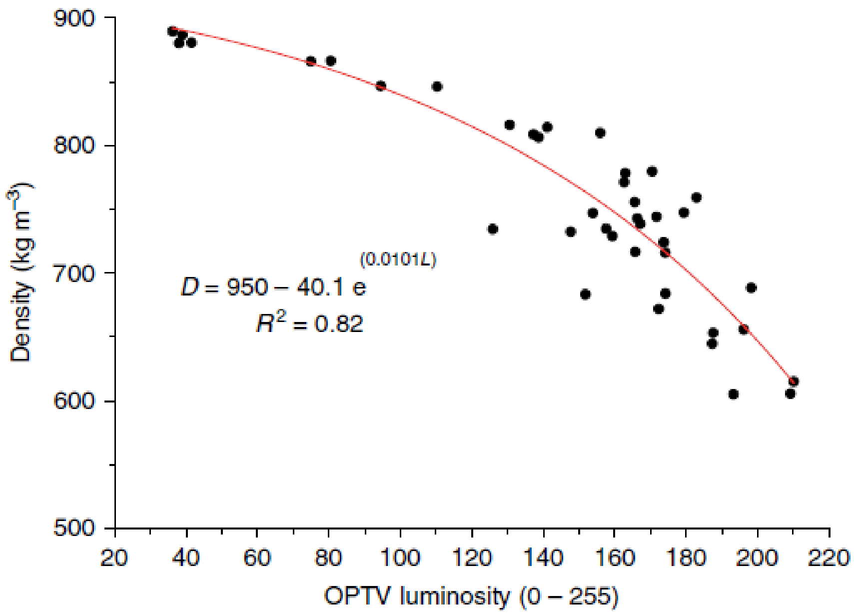

Figure 4.8. Optical televiewer density–luminosity calibration. Material density, measured gravimetrically on core samples, plotted against equivalent OPTV luminosity, both measured along a borehole located on Roi Baudouin Ice Shelf, East Antarctica. (Figure 5 in Hubbard et al., 2016)

4.2.1 Constraining variable density of ice shelves using wide-angle radar measurements

This section is a summary of Drews et al. (2016) where all references are mentioned.

Paper published in The Cryosphere, 10, 811–823, 2016, doi:10.5194/tc-10-811-2016

Title: Constraining variable density of ice shelves using wide-angle radar measurements

Authors : Reinhard Drews[1], Joel Brown[2], Kenichi Matsuoka[3], Emmanuel Witrant[4], Morgane Philippe[1], Bryn Hubbard[5], and Frank Pattyn[1]

[1]Laboratoire de Glaciologie, Université Libre de Bruxelles, Brussels, Belgium
[2]Aesir Consulting LLC, Missoula, MT, USA
[3]Norwegian Polar Institute, Tromsø, Norway
[4]Université Grenoble Alpes/CNRS, Grenoble Image Parole Signal Automatique, 38041 Grenoble, France
[5]Aberystwyth University, Aberystwyth, Wales, UK

Correspondence to: R. Drews (rdrews@ulb.ac.be)

Abstract: The thickness of ice shelves, a basic parameter for mass balance estimates, is typically inferred using hydrostatic equilibrium, for which knowledge of the depth averaged density is essential. The densification from snow to ice depends on a number of local factors (e.g., temperature and surface mass balance) causing spatial and temporal variations in density–depth profiles. However, direct measurements of firn density are sparse, requiring substantial logistical effort. Here, we infer density from radio-wave propagation speed using ground-based wide-angle radar data sets (10 MHz) collected at five sites on Roi Baudouin Ice Shelf (RBIS), Dronning Maud Land, Antarctica. We reconstruct depth to internal reflectors, local ice thickness, and firn-air content using a novel algorithm that includes traveltime inversion and ray tracing with a prescribed shape of the depth–density relationship. For the particular case of an ice-shelf channel, where ice thickness and surface slope change substantially over a few kilometers, the radar data

suggest that firn inside the channel is about 5% denser than outside the channel. Although this density difference is at the detection limit of the radar, it is consistent with a similar density anomaly reconstructed from optical televiewing, which reveals that the firn inside the channel is 4.7% denser than that outside the channel. Hydrostatic ice thickness calculations used for determining basal melt rates should account for the denser firn in ice-shelf channels. The radar method presented here is robust and can easily be adapted to different radar frequencies and data-acquisition geometries.

Full-depth density profiles are necessary for many glaciological surveys. For example, inferring basal melt rates using the hydrostatic equilibrium requires a precise estimation of the firn air content, i.e. the depth equivalent of air needed to match the depth-averaged density if all the rest of the ice column is considered as bubble-free glacial ice.

The objective of Drews et al. (2016) was to reconstruct density and ice thickness at different locations on the Roi Baudouin Ice Shelf, with the secondary goal of comparing these parameters inside and outside a 2 km wide surface channel, a specific feature of ice shelves that has recently drawn lots of attention from glaciologists working on ice-ocean interactions and their contribution to ice-shelves mass balance (Sect.1.4.1). The authors developed a new algorithm to infer density from radar wave propagastion speed using density–permittivity relations. They used a prescribed shape of the depth-density function derived from the best-fit on gravimetric measurements described in Sect. 3.1.

The algorithm was tested with ideal reflectors and applied to 4 wide-angle reflection and refraction (WARR) at 4 different depths (including the bed), with a couple reflectors used for the inversion and the other two used to validate the results. Unlike the common mid-point surveys, where both the receiver and the transmitter are moved to keep a single subsurface reflection point, the WARR geometry consists in moving only the receiver with a varying offset (Rx in Fig 4.9a,b) while keeping the transmitter (Tx in Fig 4.9a,b) fixed. These WARR measurements were repeated at 6 different sites to investigate the spatial variability of density and ice thickness.

The work achieved during this thesis contributed to Drews et al., (2016) study by providing an independent comparison for the density difference inside and outside the channel. We measured density on RBIS10 (named RBIS in Sect 3.1 and OPTV 2010 in Figs. 4.9 and 4.10) and RBIS14 (OPTV 2014 in Figs. 4.9 and 4.10) both gravimetrically (Fig. 4.7) and from the OPTV luminosity, and participated to the discussion on the significance and interpretation of the results.

Both the OPTV and the WARR methods show a ~5% higher density inside the channel, compared to the density of the ice outside the channel.

The mechanism leading to higher density is likely to be meltwater collection in the surface depression. Lenaerts et al. (2016) observed surface melt ponding near the grounding line, due to wind-albedo interaction. Higher density in the channels is suggested to result from melting and refreezing processes and inherited from upstream. This density anomaly needs to be accounted for in studies using mass budget method to estimate basal melting in ice shelves channels and in studies using hydrostatic equilibrium to derive ice thickness. Further work is however clearly needed to investigate if the density is systematically higher inside channels.

Figure 4.10 also clearly shows how powerful OPTV-derived density profiles are in discussing the fine-scale temporal variability of processes controlling firnification process at an ice shelf surface. This will be further demonstrated in the next section.

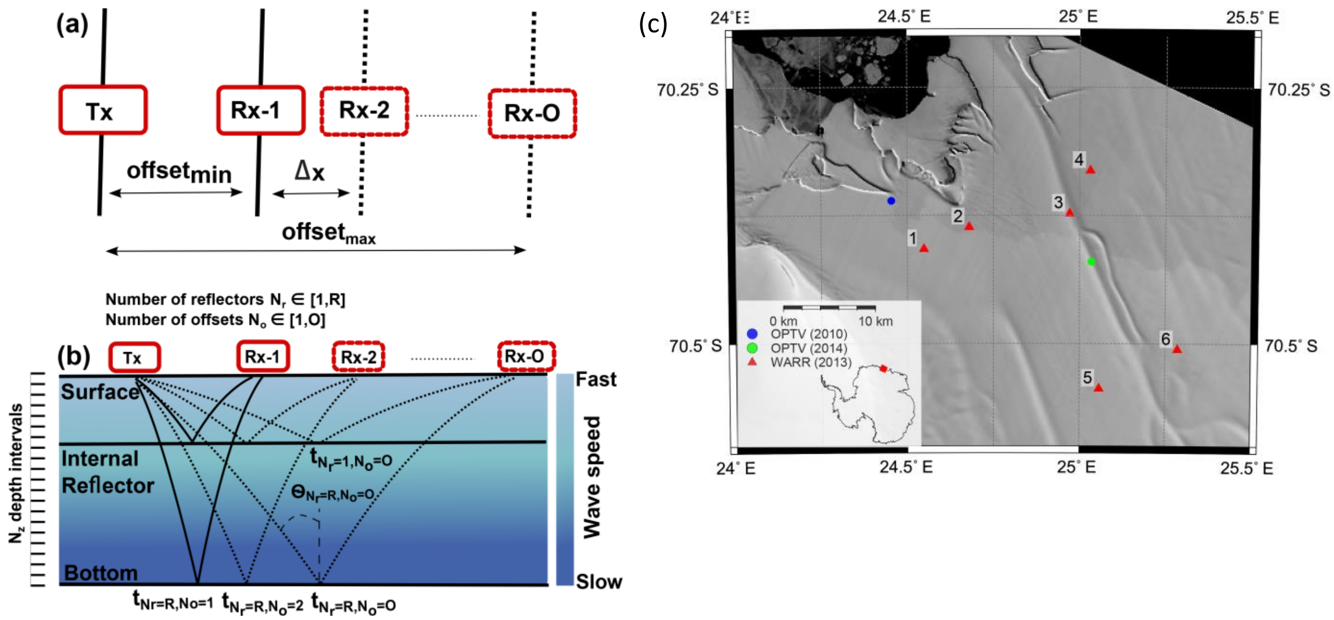

Figure 4.9 a) Plain view of the wide-angle acquisition geometry: transmitting (Tx) and receiving (Rx) antennas were aligned in parallel. While the transmitter remained at a fixed location, the receiver was incrementally moved farther away. A sketch of the corresponding ray paths is shown in (b) with a synthetic velocity–depth function represented by different shades of blue. c) Location of the wide-angle (WARR) radar sites (red triangles) relative to the boreholes of 2010 and 2014 which were used for optical televiewing (OPTV). The depressed surfaces of ice-shelf channels appear as elongated lineations in the background image (adapted from Figures 1 and 2 in Drews et al., 2016).

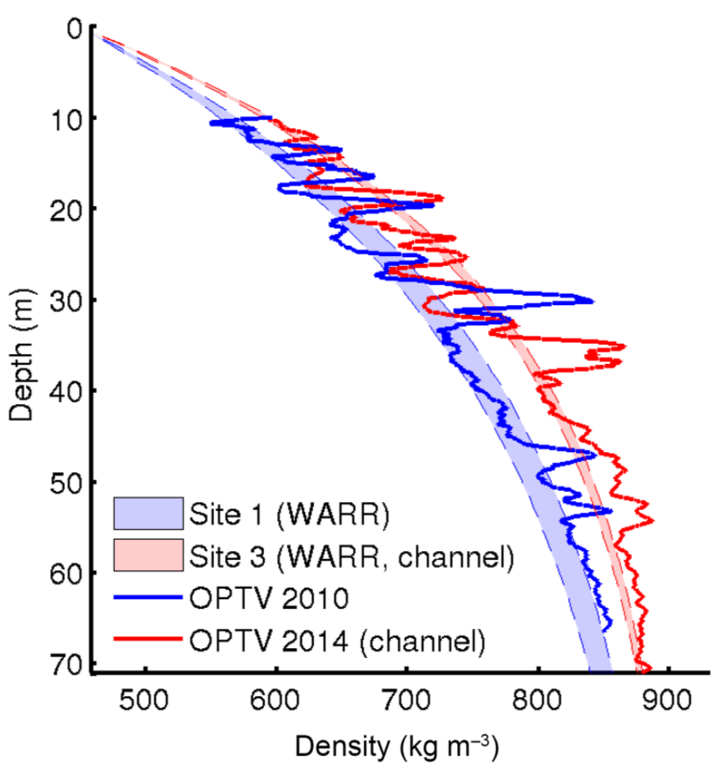

Figure 4.10 Depth profiles of density derived from WARR (dashed) and OPTV (solid). WARR data are from Sites 1 and 3, closest to the OPTV sites. Site 3 and RBIS14 are both in the trough of an ice-shelf channel (Fig. 4.9c). The envelopes of the radar derived densities correspond to the lower and upper limit of five reflector combinations used for the inversion. The OPTV logs were smoothed with a 0.5 m running mean.

4.2.2 Massive subsurface ice formed by refreezing of ice-shelf melt ponds

This section is a summary of Hubbard et al. (2016) where all references are mentioned.

Paper published in Nature Communications, 7:11897, doi: 10.1038/ncomms11897

Title: Massive subsurface ice formed by refreezing of ice-shelf melt ponds

Authors: Bryn Hubbard[1], Adrian Luckman[2], David W. Ashmore[1], Suzanne Bevan[2], Bernd Kulessa[2], Peter Kuipers Munneke[2], Morgane Philippe[3], Daniela Jansen[4], Adam Booth[5], Heidi Sevestre[6], Jean-Louis Tison[3], Martin O'Leary[2]& Ian Rutt[2]

[1]Centre for Glaciology, Department of Geography and Earth Sciences, Aberystwyth University, Aberystwyth SY23 3DB, UK.
[2]Glaciology Group, Department of Geography, Swansea University, Swansea SA2 8PP, UK.
[3]Laboratoire de Glaciologie, De´partement Ge´osciences, Environnement et Socie´te´, Université Libre de Bruxelles, Bruxelles 1050, Belgium.
[4]Alfred Wegener Institut, Helmholtz-Zentrum fu¨r Polar- und Meeresforschung D-27568, Bremerhaven, Germany.
[5]School of Earth and Environment, University of Leeds, Leeds LS2 9JT, UK. 6 Department of Arctic Geology, University Centre in Svalbard, N-9171 Longyearbyen, Norway.

Correspondence and requests for materials should be addressed to B.H. (email: byh@aber.ac.uk).

Absctract: Surface melt ponds form intermittently on several Antarctic ice shelves. Although implicated in ice-shelf break up, the consequences of such ponding for ice formation and ice-shelf structure have not been evaluated. Here we report the discovery of a massive subsurface ice layer, at least 16 km across, several kilometres long and tens of metres deep, located in an area of intense melting and intermittent ponding on Larsen C Ice Shelf, Antarctica. We combine borehole optical televiewer logging and radar measurements with remote sensing and firn modelling to investigate the layer, found to be ~10°C warmer and ~170 kg m^{-3} denser than anticipated in the absence of ponding and hitherto used in models of ice-shelf fracture and flow. Surface ponding and ice layers such as the one we report are likely to form on a wider range of Antarctic ice shelves in response to climatic warming in forthcoming decades.

Hubbard et al. (2016) used OPTV and GPR to investigate the ice structure of Larsen C ice shelf (LCIS, Fig. 4.11a), located on the Antarctic Peninsula, a region influenced by intense surface melting and intermittent ponding. They found a massive body of ice, at least 16 km across, several kilometres long and tens of metres deep, evidenced by a very specific signal in the borehole optical properties 2.9 m below the surface. Compared to the DIR (IC12) OPTV log, the LCIS shows a completely dark zone until 45 m and a lighter zone with horizontal dark layers below that (Fig 4.11c). The upper layer (2.9 m to 45 m) is interpreted as corresponding to pond ice, i.e. formed by refreezing of ice-shelf melt ponds and the bottom layer is interpreted as infiltration ice, i.e. formed by meltwater percolating into underlying firn. The presence of these ice layers has been investigated by GPR on an area of almost 100 km² and they found evidence that the whole area is influenced by melting and that the presence of the subsurface ice is widespread. Its spatial extension is inferred from the strong near surface reflector observed in the GPR data, interpreted as the upper surface of the ice layer. However, GPR do not allow to distinguish between pond ice and infiltration ice.

The authors used a one dimensional firn densification and hydrology model, driven by surface fluxes and regional temperature data to explain the origin of that ice layer. The model simulates a melt to accumulation ratio of snow and predicts the variation of density with depth accordingly. The depth at which the massive ice layers is found is exactly reproduced by the model. Satellite images also show consistent evidences of ponding during the corresponding period (2001-2009).

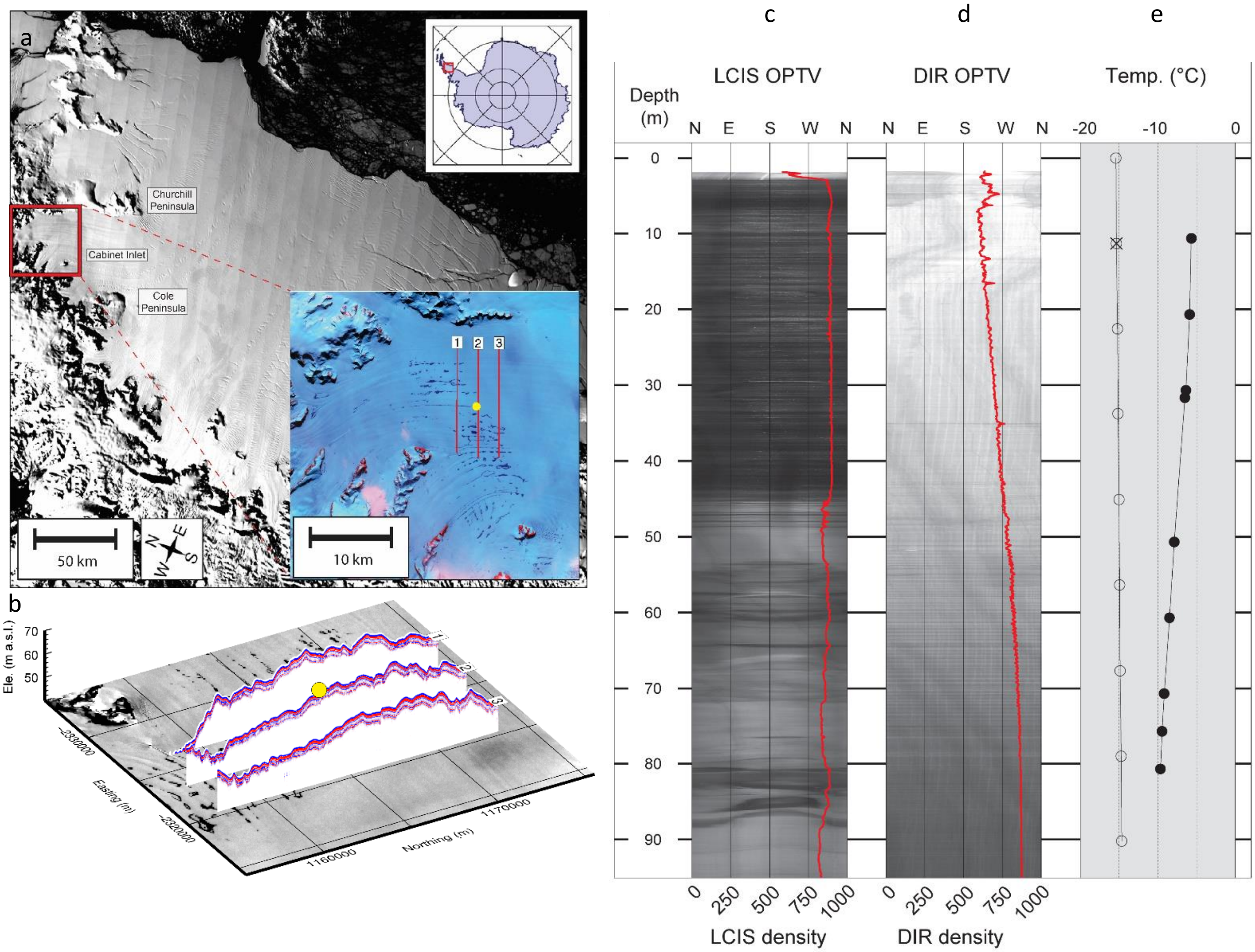

Figure 4.11. (a) Cabinet Inlet (Larsen C ice shelf) with Landsat expansion on 31st December 2001 showing surface ponding (dark patches). The borehole location is indicated by a yellow dot and the 200-MHz GPR transects presented in panel b are shown in red lines. (b) GPR profiles showing near-surface reflectors (c) OPTV log of the LCIS borehole. This raw log is of the complete borehole wall, unrolled to progress north—east—south—west—north from left to right. (d) OPTV log of the DIR borehole, unaffected by significant melting. Density profiles derived from OPTV luminosity are superimposed as red lines on both OPTV logs. (e) Englacial temperatures (i) measured by borehole thermistor string (solid dots), (ii) that would normally be used in an ice-shelf model for this site (open circles), and (iii) predicted by our firn model at a depth of 11m (cross). Adapted from Hubbard et al. (2016).

Our contribution to this study was to make the calibration for the new probe used on LCIS with data from RBIS14, described in Sect. 4.2.1. This calibration allowed the estimation of the density of the massive ice layer to be about 870 kg m^{-3}, 24% higher than the density used in an LCIS model (Jansen et al., 2010), which has implications for the calculation of ice-shelf thickness from remote sensing. It also allowed to quantify the difference in density between the upper unit, with a mean density of 888 kg m^{-3} compared to the underlying ice layer (854 kg m^{-3}). We calculated the root mean square error on different density ranges and participated to the discussion on the significance of the results.

The authors also report that the ice body is warmer compared to the temperature predicted by the firn model, even when percolating meltwater is included (Fig 4.11c). This is due to the latent heat released by the refreezing of ponded meltwater. This property, together with the higher density of that ice layer has potential implications for ice-shelf stability. However, its influence can be interpreted in two very different ways. On the one hand, this ice is less viscous due to its higher temperature, which can accelerate its flow and reduce back-stress, therefore increasing shear stresses along the flow at the margin of that ice body. On the other hand, this ice could be more resistant to tensile fracture and reduce the occurrence of crevasses, generally perpendicular to the flow. Another effect that needs to be considered is the coincidence of longitudinal troughs with basal channels, which can lead to the formation of crevasses. Ice-flow modelling is required for further investigation. This has important implications since the area influenced by melting is likely to extend with climate change, and has been recently evidenced in East Antarctica (Lenaerts et al., 2016).

4.3 IceCon : Constraining ice mass changes in Antarctica

The IceCon multidisciplinary project has led to interesting results concerning ice rises, ice shelves and pinning points. They are formed during the transition between glacial and interglacial periods (Favier & Pattyn, 2015) and slow down the process of deglaciation. Their geometry needs to be correctly mapped because even the smallest pinning points can significantly buttress the ice flow (Berger et al., 2016; Favier et al., 2016). This is not the case in current projections of future contributions of Antarctica to sea level rise (Church et al., 2013).

Ground penetrating radar and ice sheet modelling were combined to determine that the DIR divide elevation is close to steady-state and has potentially undergone modest surface lowering in the past (Drews et al., 2015). The timing of deglaciation is now better constrained, as the chronology of local flow patterns (Raymond arches amplitude) show that the divide position has been stable for at least 5000 years and that the flow remained local at least since the Mid-Holocene (Drews et al., 2015).

Together with the very low signal of post-glacial rebound measured by the GNSS stations installed between the Sor Rondane Mountains and the coast during this project (IceCon final report: Pattyn et al., 2017), these findings confirm that the DIR was not overridden by the Antarctic Ice Sheet during the Last Glacial Maximum, similar to what earlier modelling studies suggested (Pattyn et al., 1989, 1992) .

Measuring the post-glacial rebound directly on the ice was another target of the IceCon project (Eq. 1.1, p. 25). However, our results have shown that the uncertainties associated with this method are higher than the isostatic movement to be measured. More precise measurements of all parameters (density, SMB and vertical velocity) will need improvement of the methods used and cross-validation with the newest radar technologies to record vertical velocity down to the bedrock (e.g. ApRES, autonomous phase-sensitive radio-echo-sounding). These measurements will also allow us to characterize the spatial variability at a regional scale.

4.4 Ice core evidence of SMB dissymmetry around ice rises: preliminary results

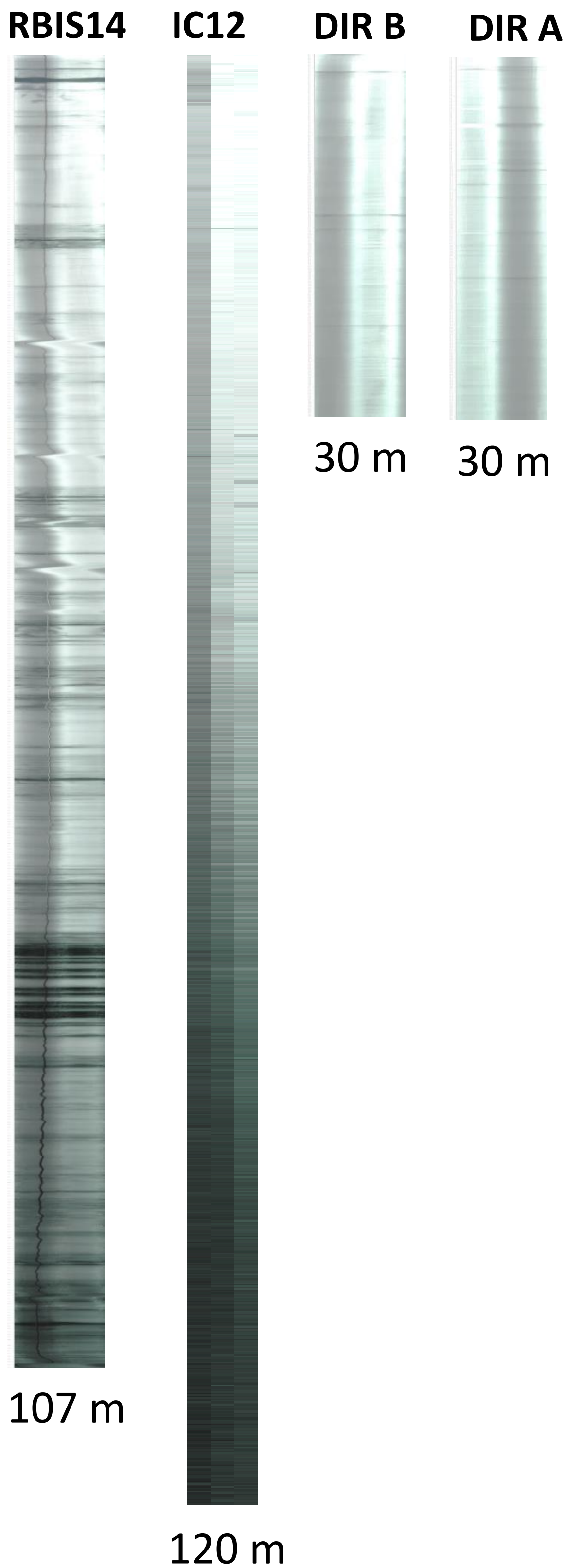

A side goal of the IceCon Project, developed during the second field expedition (2014), was to confirm the SMB asymmetry detected by radar measurements (Sect. 4.1.1) and predicted by atmospheric modelling (Sect. 4.1.2).

Figure 4.12 shows the OPTV logs obtained during the 2012 and 2014 field season in 4 boreholes. The RBIS14 ice core was drilled on the channel in the ice shelf and its interest has been discussed in Section 4.2. In this section, we will focus on the differences between the 3 boreholes drilled on the DIR: IC12 at the divide, DIR A and DIR B, both 2 km away from the divide on a line corresponding to the wind direction, with DIR B on the upwind slope and DIR A on the downwind slope. The DIR A and DIR B boreholes were analyzed both with OPTV logging and using stable isotopes analyses on the damaged ice cores.

In principle, the OPTV logs could allow us to compare the three sites: IC12, DIR A and DIR B, in terms of density. New brightness density proxy calibration was not attempted because of the ice core damages. The IC12 calibration (DIR in Hubbard et al., 2013, Sect. 3.1) has been used instead.

The water stable isotopes measurements could have been potentially affected by the ice core warming/melting during transport. However, visual examination of the core suggested that the central part of the core remained unaffected. These were used for annual layer identification based on water stable isotope measurements.

Figure 4.12: OPTV logs of 4 boreholes: RBIS14 = Roi Baudouin Ice Shelf in longitudinal depression; IC12 = 2012 120 meters ice core at the summit of Derwael Ice Rise, revisited in 2014; DIR A = ~2 km downwind from IC12; DIR B = ~ 2 km upwind from IC12 – see Fig. 2.1 for location.

Density and SMB were studied by Courrier (2016) who measured water stable isotopes at 5 cm resolution on DIR A and DIR B. This master's thesis confirmed that SMB is higher on the upwind side (DIR B, mean = 713 ± 19 kg m^{-2} a^{-1}) than on the downwind side (DIR A, mean = 623 ± 42 kg m^{-2} a^{-1}). These SMB values are the same order of magnitude as those obtained from radar measurements (Fig. 4.4).

As expected, density is higher on the downwind site (DIR A, Fig.4.13) This is due to the difference in SMB and wind regime between the two flanks. In addition to a lower SMB, DIR A is also more exposed to erosion by the wind, which could favor icy crust formation. Indeed, Fjøsne (2014) showed that the distribution of the samples with icy layers at the summit of Derwael (IC12) is slightly displaced towards lower values of $\delta^{18}O$ than samples without ice layers, suggesting that these icy layers are located in the "winter" layers. This can be due to snow sublimation by relatively dry air on the downwind side (Matsuoka et al., 2015), although modelling suggests that sublimation should be relatively small on DML ice rises (Lenaerts et al., 2014).

In terms of submergence velocity, a comparison between DIR A and IC12 was attempted (Fig. 4.14), as their two OPTV logs show a few similarities (visual markers numbered between 1 and 13 in Fig. 4.14). Note that, to use the same probe as for the other sites, the IC12 log considered here is the one revisited in 2014. Therefore, it has been shifted downwards by 2.83 m to account for the depth of snow that was excavated to recover the 2012 borehole. Once that shift has been applied, the first marker is lower in IC12 than DIR A, consistent with a slightly higher SMB at IC12. However, the offset between the two logs reduces until 21 m, where the markers in DIR A become deeper than those in IC12. If we assume that the SMB spatial pattern is exactly constant from year to year, the offset we observe between DIR A density log and IC12 density log could be attributed to a higher submergence velocity in DIR A, compared to the IC12 site. This is consistent with DIR A being situated more towards the flanks of the ice rise and IC12 being situated closer to the divide. The Raymond effect induces lower velocities at the divide, due to the anisotropic rheology of the ice. However, the SMB pattern is not exactly constant from year to year and the resolution of the radar data linking the three sites is

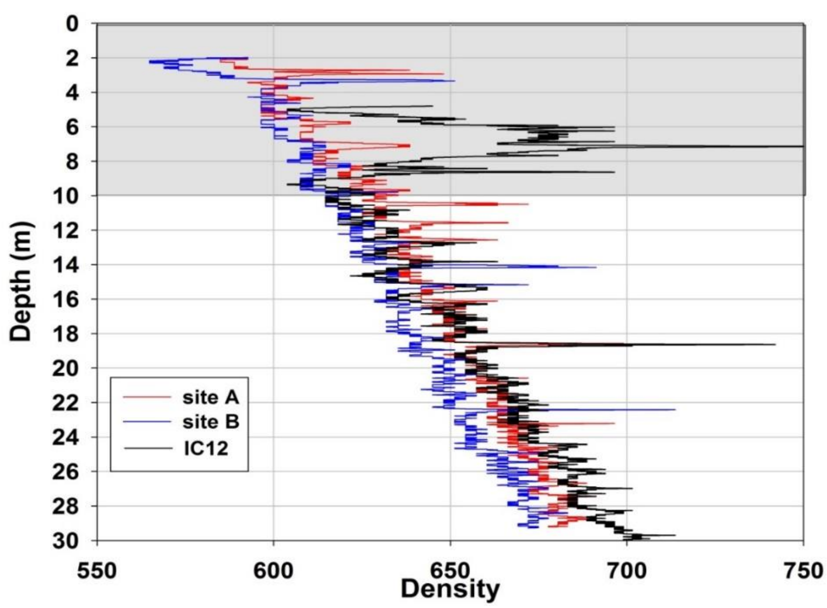

Figure 4.13: Density profiles at DIR A (site A), DIR B (site B) and DIR-IC12. All profiles obtained from the OPTV brightness-density proxy using Eq. 3.1.2 (Eq. 2 in Hubbard et al., 2013). Grey-area denotes upper 10 meters where OPTV derived densities are potentially not reliable. The DIR-IC12 curve has been shifted downwards by 2.83 m (see text for explanation).

insufficient to account for this temporal variability in SMB. Spatial variations in submergence velocities could be further investigated using pRES. This technique has indeed a wider spatial coverage (Kingslake et al., 2014) despite a lower vertical resolution (Sect. 3.3).

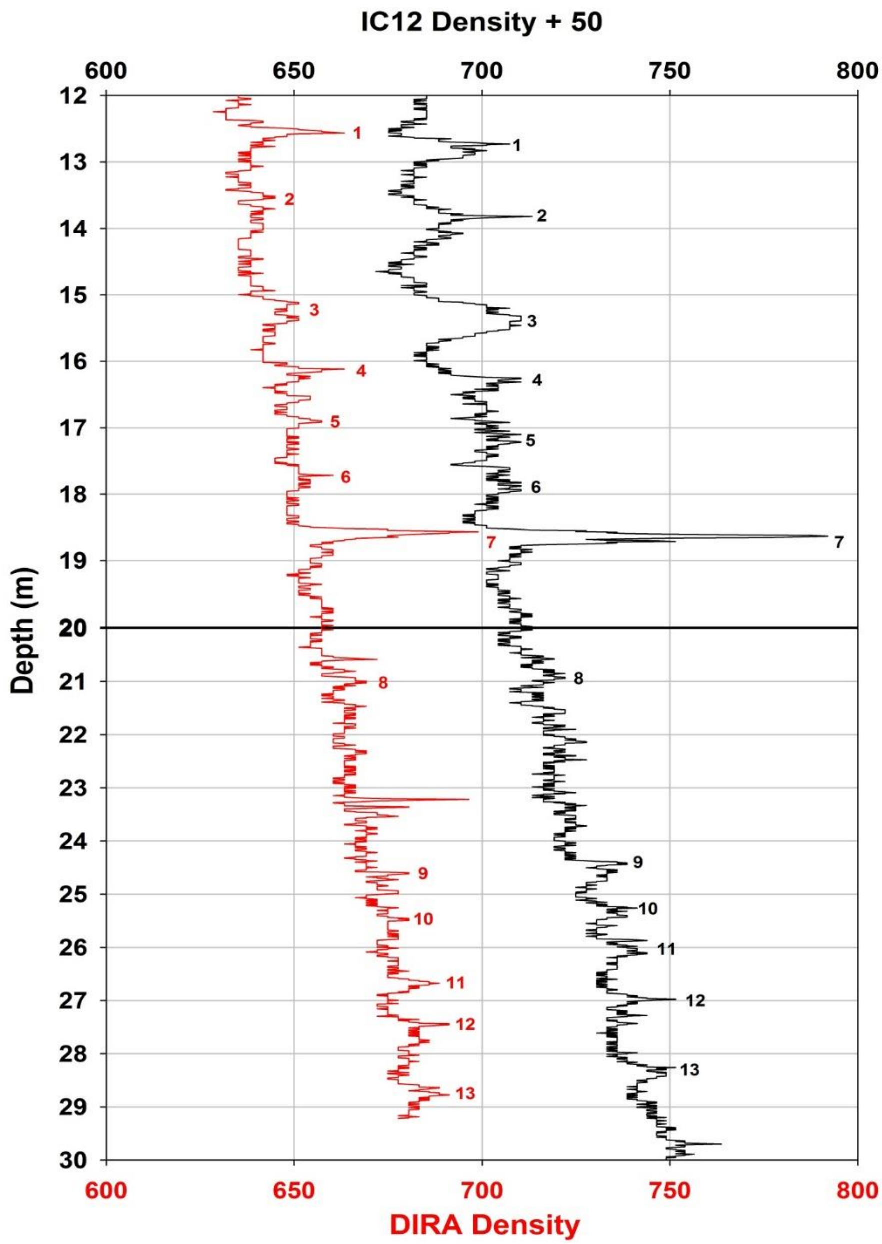

Figure 4.14: Density profiles at DIR A (site A) and IC12- enlargement. All profiles obtained from the OPTV brightness-density proxy using Eq. 3.1.2 (Eq. 2 in Hubbard et al., 2013). The IC12 curve has been shifted downwards by 2.83 m (see text for explanations), and rightwards (by adding 50 of density) for clarity. Numbers relate to visually correlated peaks/features.